Nickel mass balance and isotopic records in a serpentinic weathering profile: Implications on the continental Ni budget

A.L. Machado, J. Garnier, Gildas Ratié, E. Guimaraes, G. Monvoisin, C. Cloquet, C. Quantin

▶ To cite this version:

A.L. Machado, J. Garnier, Gildas Ratié, E. Guimaraes, G. Monvoisin, et al.. Nickel mass balance and isotopic records in a serpentinic weathering profile: Implications on the continental Ni budget. Chemical Geology, 2023, 634, pp.121586. 10.1016/j.chemgeo.2023.121586 . insu-04125164

HAL Id: insu-04125164
https://insu.hal.science/insu-04125164v1

Submitted on 12 Jun 2023

HAL is a multi-disciplinary open access archive for the deposit and dissemination of scientific research documents, whether they are published or not. The documents may come from teaching and research institutions in France or abroad, or from public or private research centers.

L'archive ouverte pluridisciplinaire **HAL**, est destinée au dépôt et à la diffusion de documents scientifiques de niveau recherche, publiés ou non, émanant des établissements d'enseignement et de recherche français ou étrangers, des laboratoires publics ou privés.

Journal Pre-proof

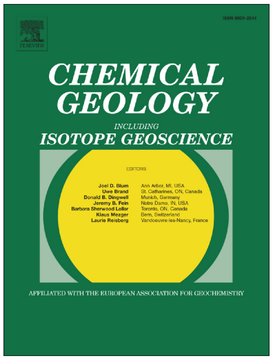

Nickel mass balance and isotopic records in a Serpentinic weathering profile: Implications on the continental Ni budget

A.L. Machado, J. Garnier, G. Ratié, E. Guimaraes, G. Monvoisin, C. Cloquet, C. Quantin

PII: S0009-2541(23)00286-3

DOI: https://doi.org/10.1016/j.chemgeo.2023.121586

Reference: CHEMGE 121586

To appear in: *Chemical Geology*

Received date: 3 October 2022

Revised date: 2 June 2023

Accepted date: 5 June 2023

Please cite this article as: A.L. Machado, J. Garnier, G. Ratié, et al., Nickel mass balance and isotopic records in a Serpentinic weathering profile: Implications on the continental Ni budget, *Chemical Geology* (2023), https://doi.org/10.1016/j.chemgeo.2023.121586

This is a PDF file of an article that has undergone enhancements after acceptance, such as the addition of a cover page and metadata, and formatting for readability, but it is not yet the definitive version of record. This version will undergo additional copyediting, typesetting and review before it is published in its final form, but we are providing this version to give early visibility of the article. Please note that, during the production process, errors may be discovered which could affect the content, and all legal disclaimers that apply to the journal pertain.

© 2023 Published by Elsevier B.V.

Journal Pre-proof

Nickel mass balance and isotopic records in a Serpentinic weathering profile: implications on the continental Ni budget

***A.L. Machado*[a], *J. Garnier*[a,b*], *G. Ratié*[c], *E. Guimaraes*[a], *G. Monvoisin*[d], *C. Cloquet*[e], *C. Quantin*[d]**

[a] University of Brasilia, Geosciences Institute, Brasilia-DF, Brazil.

[b] Laboratoire Mixte International IRD/UnB, LMI OCE « Observatoire des changements Environnementaux », Institut de Recherche pour le Développement / University of Brasilia, Brasilia, Brazil

[c] Univ. Orléans, CNRS, BRGM, ISTO, UMR 7327, F–45071, Orléans, France.

[d] UMR 8148 GEOPS, Université Paris Saclay – CNRS , 91405 Cedex, France.

[e] CRPG, UMR 7358, CNRS-Université de Lorraine, 15, rue Notre-Dame-des-Pauvres, BP20, 54501, Vandœuvre-lès-Nancy, France.

*Corresponding author. e-mail: garnier@unb.br

Journal Pre-proof

Journal Pre-proof

ABSTRACT

During serpentinite rock weathering, Ni is concentrated in the regolith owing to residual and secondary enrichment, forming a Ni-rich deposit under tropical conditions. This study presents geochemical, isotopic, and mineralogical data for Ni from the Serra do Puma Complex (SPC) weathering profile in Carajas (Brazil). The Ni fluxes, redistribution, and Ni isotopic fractionation magnitudes were quantified along the entire weathering profile: rock, saprock, lower and upper saprolite, and limonite. The results show that chlorite and serpentine are the primary Ni-scavenging phases in saprolite, whereas Fe oxyhydroxides are the main Ni-hosting minerals in the limonite unit. The mass balance model confirmed a global Ni gain at the weathered profile scale, with larger Ni enrichment in the upper saprolite. The isotopic dataset obtained in this study contributes greatly to the knowledge of the current Ni cycle on regional and global scales. The detailed insights into Ni isotopes in the SPC, coupled with chemical and mineralogical composition, allow for the first time a Ni mass balance and Ni isotopic values for an entire weathering profile in an Amazonian context. The Ni isotopic profile agrees with the preferential retention of light Ni isotopes in the residual material relative to the parent rock during weathering processes, with the $\Delta^{60}Ni_{\text{limonite-saprock}}$ of −0.72‰. In the SPC, major isotopic fractionation was notably recorded during saprolitization, while limonitization was accompanied by an overall Ni loss without significant Ni isotopic fractionation. As already observed in previous studies, heavier Ni isotopes, preferentially leached during weathering processes, can be further mobilized downward and lost from the profile or incorporated in secondary minerals in the saprolite and limonite sections. The Ni isotopic mass balance model indicated that the Ni loss from the weathered serpentinite profile was isotopically heavy, in agreement with the isotopically heavier composition of the dissolved load of Amazonian rivers. The isotopically light Ni pool, associated with the significant Ni gain encountered in the upper saprolite, is notable in the SPC weathering profile and confirms the existence of a light Ni isotope reservoir in the continent.

Journal Pre-proof

1. Introduction

The laterite nickel (Ni) deposits developed upon serpentinite rocks, known to constitute around 70% of the world's Ni resources (Butt and Cluzel, 2013), are one of the main Ni sources for rivers and coastal ecosystems (Noel et al., 2017, Merrot et al., 2022). Laterite Ni are deposits formed by the prolonged intense weathering of ultramafic rocks, such as peridotite or serpentinite, under actual or past humid tropical conditions (Golightly, 2010; Butt and Cluzel, 2013). Weathering processes lead to the leaching of the most mobile elements of the bedrock (Mg and Si) and the enrichment of less mobile elements, such as Fe, Cr, Ni, Mn, or Co (Freyssinet et al., 2005; Golightly, 2010; Butt and Cluzel, 2013). A typical weathering profile generally consists of serpentinite rock overlain by saprolite and ferruginous (often called limonitic) horizons containing secondary minerals enriched in Ni, such as clay minerals, and Mn or Fe oxyhydroxides (Freyssinet et al., 2005, Butt and Cluzel, 2013). The Ni-ore types are commonly classified as oxide, clay silicate, or hydrous Mg silicate deposits according to the main Ni scavengers, i.e. fine-grained secondary minerals such as Fe oxyhydroxides, saponite and smectite, serpentine, chlorite, and sepiolite (i.e., garnierite), respectively (Brand et al., 1998; Butt and Cluzel, 2013; Fan and Gerson, 2015).

The genesis of laterite Ni-deposits in tropical conditions has been extensively investigated in Brazil (Colin et al., 1990; Silva and Oliveira, 1995; Ratié et al., 2018), Colombia (Gleeson, et al., 2004), Indonesia (Fu et al., 2014; Fan and Gerson, 2015), Cuba and the Dominican Republic (Gleeson et al., 2004; Aiglsperger et al., 2016; Domènech et al., 2022), New Caledonia (Dublet et al., 2012; Ulrich et al., 2019), Philippines (Tupaz et al., 2020; Aquino et al., 2022), and Myanmar (Sun et al., 2022). During weathering, Ni is relatively soluble and may be strongly adsorbed, incorporated, and coprecipitated into Mn and Fe oxyhydroxides in the upper layer, which are rich in goethite, hematite, and Mn oxides (Elias, 2002; Freyssinet et al., 2005; Golightly, 2010; Dublet et al., 2012; Butt and Cluzel, 2013; Ugwu et al., 2019). Part of the Ni is then leached from the overlying oxide zone and incorporated into the underlying hydrous silicate saprolite layer rich in garnet minerals (Ni-bearing serpentines, chlorites, and talc) (Elias, 2002; Gleeson et al., 2004; Villanova-de-Benavent et al., 2017).

The understanding of the behavior of Ni in regolith developed on serpentinic rocks has been completed by exploring its isotopic systematics applicable as geochemical tracers (Estrade et al., 2015; Ratié et al., 2015; 2018; Pędziwiatr et al., 2018; Spivak-Birndorf et al., 2018). Previously published data suggest that the serpentinization process does not significantly affect δ^{60}Ni values in peridotites (Gall et al., 2013; Gueguen et al., 2013; Estrade et al., 2015; Ratié et al., 2015). In contrast, intense Ni isotopic fractionation was observed during the Ni speciation changes related to

Journal Pre-proof

Journal Pre-proof

biogeochemical reactions during weathering. The preferential enrichment of light Ni isotopes in the solid phase, such as adsorption onto clay minerals of type 2:1 and Mn and Fe oxyhydroxides, has been confirmed (Wasylenki et al., 2015; Wang and Wasylenki, 2017; Gueguen et al., 2018; Ratié et al., 2015; 2018; Spivak-Birndorf et al., 2018; Neubeck et al., 2021; Sorensen et al., 2020). They revealed various Ni isotope fractionation factors (Komárek et al., 2022) during interfacial reactions, making them distinguishable and useful for a better understanding of Ni cycling at the Earth's surface.

Ni isotopic systematics during weathering processes have been investigated in two deep Ni lateritic profiles in the Barro Alto laterite Ni-deposit (Goiás State, Brazil). In this study, the lateritic profile of the Amazonian Basin, which is responsible for almost 20% of the world's freshwater discharge into the ocean (Dai and Trenberth, 2002) has been investigated. Considering the importance of serpentinite outcrops in the Ni cycle on a global scale, the Puma deposit of Carajas (Pará State, Brazil) provides a crucial environment for studying Ni geogenic sources through laterization and remobilization in the Amazonian Basin. Therefore, the present study focused on the behavior and isotopic trend of Ni during the formation of laterite Ni-deposits in the Carajás Mineral Province, northern Brazil (i.e., Jacaré-Jacarezinho, Vermelho, and Onça-Puma).

This study details the genesis and dynamics of Ni in the Serra do Puma weathering profiles. The proposed mass balance model allows the quantification of mass loss, gain, and Ni redistribution during chemical weathering. The underlying idea is to discuss the Ni ore formation in a Carajas laterite Ni-deposit for the first time, presenting a complete overview of the distribution and concentration of Ni along the Puma serpentinite weathering profile, its relationship with mineralogy, and the formation of a light Ni isotope reservoir. Additionally, detailed insights into the Ni isotopes in serpentinite rock, coupled with the chemical and mineralogical composition, allow for the first Ni mass balance and Ni isotopic values over an entire weathering profile in a tropical context. The results obtained can be discussed relative to the riverine Ni composition of major rivers draining into the Amazon basin.

2. Geological settings

The Carajás Mineral Province (CMP) represents the oldest and best-preserved crustal segment of the Amazonian Craton. It is located in the southeastern portion of Pará State in northern Brazil and is one of the largest mineral provinces on Earth (Vasquez et al., 2008). The CMP includes two major tectonic domains: the Mesoarchean Rio Maria Domain (RMD) in the south, and the Neoarchean Carajás Domain (CD) in the north (Araújo et al., 1988; Araujo and Maia, 1991; Vasquez et al., 2008). A poorly defined zone characterized by regional EW faults, designated as transition subdomains, separates these two domains (Feio et al., 2013). Potential laterite Ni-deposits associated with serpentinized dunites are mainly located in the CD, including the Cateté Intrusive Suite, Serra do Puma Complex (SPC), and Serra da Onça Complex (SOC) (Macambira, 1997; Tassinari and Macambira, 1999; Macambira and Ferreira Filho, 2002).

The Cateté Intrusive Suite corresponds to a set of large-to-medium-sized, layered, and anorogenic mafic-ultramafic intrusions located in the western portion of the CMP in the southern part of the CD (Macambira and Vale, 1997). Macambira and Ferreira Filho (2002) reported that these layered intrusions have thick ultramafic zones at the base of the igneous stratigraphy, where laterite Ni-deposits developed over the serpentinized dunite and peridotite. The Geology of the Cateté Intrusive Suite was broadly characterized throughout the 90s and the 2000s (Macambira and Vale, 1997; Macambira and Ferreira Filho, 2002; Ferreira Filho et al., 2007; Teixeira et al., 2015; Mansur et al., 2016). Rosa (2014) provided geological and petrological information that allowed the characterization of the Serra do Puma and Serra da Onça complexes in the context of the mafic-ultramafic magmatism of the CMP.

The SPC consists of a 25 km long and less than 3 km wide SW–NE-trending layered intrusion with a Lower Border Group (LBG), an Ultramafic Zone (UZ), and a Layered Zone (LZ) (**Figure 1**; Rosa, 2014). The LBG forms a thin zone of gabbroic rocks (Cpx + Pl cumulate) located on the northern border of the SPC and at the hill base. The UZ formed an elongated hill consisting mainly of dunite, interlayered peridotite, and clinopyroxenite. The dunite is extensively serpentinized and weathered. The LZ consists mainly of gabbro with abundant interlayered peridotite and clinopyroxenite. The SPC hill is sustained by silica-rich laterite (Rosa, 2014).

The Serra do Puma and Serra da Onça layered intrusions are best known for hosting VALE’s world-class laterite Ni-deposit in the CMP, the Onça-Puma Project, which includes an open-pit mine and an Fe-Ni smelter (Rosa, 2014). The supergene ore in the SPC corresponds to the Ni-hydrated silicate type, with the garnierite ore type as the main nickel-bearing phase and subordinate Ni-chlorite and Ni-limonite phases (Vasquez et al., 2008). The Puma-Onça Project produced 2,200 tons of nickel contained in ferronickel in the third quarter of 2021 (Vale 1Q21 Report: in www.vale.com). Although the geology of the Carajás mafic-ultramafic complexes has been extensively described in the literature (Macambira, 1997; Macambira and Ferreira Filho, 2002; Ferreira Filho et al., 2007; Rosa, 2014; Mansur et al., 2016), there is a lack of data on the formation of its lateritic regolith, particularly regarding Ni enrichment.

Journal Pre-proof

Journal Pre-proof

The Supporting Information (SI) provides additional information on the Carajas geology (SI and **Figure S1**).

3. Material and methods

3.1 Sampling and sample preparation

A diamond drill core approximately 200 m long, provided by VALE, was sampled to collect rock chips through the entire regolith, that is, from the bedrock to the surface. Twenty-seven samples were collected according to depth and macroscopic descriptions (color, texture, and structure) up to 45 m **(Figures S2 to S5).** In addition, two rock samples identified as serpentinite were collected between 180 and 200 m. All samples were air-dried, homogenized, and powdered using a mortar and pestle.

3.2 . Analytical procedures

3.2.1 Mineralogical analyses

Thin sections of serpentinite, saprock, and saprolite samples (n=18) were analyzed for structure and mineralogy using transmitted light microscopy.

The mineralogical composition of the powdered solid samples was determined by X-ray Diffraction (XRD; Rigaku®, Ultima IV diffractometer) using Ni-filtered Cu-Kα radiation under 30 kV and 10 mA and a graphite monochromator. The XRD patterns were recorded from 2ϴ values of 2º to 80º with a scanning speed of 2º/min. Minerals were identified using Materials Data Inc. (MDI) JADE 9.0 software.

The XRD patterns were obtained for the finely crushed powders (< 2 mm fraction, total fraction) and a selection of clay fractions (< 2 µm). The clay fraction was separated by dispersing 5 g of the powdered material in distilled water. The mixture was then centrifuged at 750 rpm for 7 min, and the suspension was transferred to another recipient and centrifuged at 3,000 rpm for 30 min to decanter the clayey fraction. Finally, these samples were subjected to solvation with ethylene-glycol and heating to differentiate clay minerals with d = 14 Å.

3.2.2 Total digestion of solid samples and analysis

For major and relevant minor elements, such as Fe, Mg, Si, Al, Cr, Mn, Ti, and Zr, the samples were melted using alkaline fusion ($LiBO_2$) followed by re-dissolution in 2M HCl, and the

Journal Pre-proof

Journal Pre-proof

concentrations were determined by inductively coupled plasma-optical emission spectrometry (ICP-OES (Inductively Coupled Plasma - Optical Emission Spectrometry, 5100, Agilent, USA).

Minor and trace element concentrations were determined for all samples after acid digestion. Approximately 100 mg of dry material was digested in a Savillex® PFA reactor using a 4-step acid digestion ($HClO_4$, HF, HCl, HNO_3, and H_2O_2) method. After proper dilution, concentrations were determined using inductively coupled plasma mass spectrometry (ICP-MS, Q-Thermo Scientific) in the HydroScience Montpellier laboratory (Montpellier, France). For ICP-MS analysis, an internal solution containing Be, Sc, Ge, Rh, and Ir was added online to the samples to correct for signal drifts. The Ce anomaly Ce/Ce* was calculated using the linear extrapolation $Ce^*/Nd_{CI} = 2(Pr_{CI}/Nd_{CI})-1$ proposed by Barrat et al., 2023.

Quality Assurance (QA) and Quality Control (QC) for both ICP-MS and ICP-OES analyses were checked using certified reference materials: BHVO-2 (volcanic basalt) and NIST SRM 2709a (San Joaquin Soil) for total concentration digestion, and NRC (SLRS-6) (CRM Environment Canada) for digestion solution analysis control of ICP-MS analyses. The accuracy of the standard samples averaged within ± 5% of certified values.

3.2.3 Dithionite Citrate Bicarbonate extractions

Reducible Fe oxides were extracted following the DCB extraction procedure (Mehra and Jackson, 1960) with a 0.3M sodium tricitrate and 1M sodium bicarbonate solution in 1 g of dry sediment at 80 ºC for 15 min, then 1 g of solid dithionite (sodium hydrosulfite) was added to the solution at 80ºC for 30 min. Details of the procedure are available in Supplementary Information.

The Ni, Fe, Mn, and Cr concentrations in the DCB-extracted solutions were determined using ICP-OES (5100, Agilent, USA). Reference material BCR-701® was used to ensure the quality of the analytical procedure.

3.2.4 Nickel isotopic analyses

The Ni chemical purification procedure for the samples was based on a two-step chromatographic separation procedure, which is fully described by Estrade et al. (2015). Following sample digestion, 2 µg of Ni were taken up with 6M HCl for the chemical separation of Ni. A Ni double spike (61Ni and 62Ni) was added to the samples at a spike/sample ratio of 1.15 (Estrade et al., 2015). Spikes and samples were equilibrated, dried, and re-dissolved before being passed through a series of resins, that is, AG1-X8 (BioRad 100–200 mesh), which retains Fe, Zn, and a high amount of Co and Cu (Moynier et al., 2007), and a Ni-specific resin (Triskem Inc., France), which retains Ni

Journal Pre-proof

Journal Pre-proof

as an insoluble Ni-dimethylglyoxime complex at pH 8–9. Finally, the eluted Ni solution was evaporated and taken up in 2% HNO_3.

Nickel isotopic compositions were measured using the Thermo-Scientific™ Neptune Plus MC-ICP-MS installed at CRPG, Nancy, France, according to Estrade et al. (2015). The isotope ratios were normalized to ^{58}Ni and reported as δ^{60}Ni relative to SRM-986 (NIST Ni Isotopic Standard) (Eq. 1):

$$\delta^{60}Ni = \left(\frac{\left(\frac{^{60}Ni}{^{58}Ni}\right)_{sample}}{\left(\frac{^{60}Ni}{^{58}Ni}\right)_{stdSRM-986}} - 1 \right) \times 1000 \; (1)$$

The reference materials Nod-A-1 and Nod-P-1 (USGS) have been digested following the same procedure as soils samples (n = 3 each) and measured as external standards in the measurement sessions, obtaining 1.07 ± 0.07‰ (2 SD, n = 3) for Nod-A1 and 0.38 ± 0.07‰ (2 SD, n = 3). These values are indistinguishable from previous measurements conducted over three years using identical analytical sequences and have been performed in various laboratories (e.g. Cameron et al., 2009; Gall et al., 2013; Gueguen et al., 2013; Ratié et al., 2015; Revels et al., 2021; Rasti et al., 2022).

3.3 . Enrichment Factor and computed gains and losses

The Ni enrichment factor (EF_{Ni}) was calculated using Zr as the conservative element (Eq. 2). Zr was selected owing to its low mobility and conservative characteristics during humid weathering processes (Nesbitt and Wilson, 1992).

$$EF_{Ni} = \frac{[Ni]/[Zr]_{sample}}{[Ni]/[Zr]_{parent\ rock}} \quad (2)$$

Where $[Ni]/[Zr]_{sample}$ and $[Ni]/[Zr]_{parent\ rock}$ are the concentration ratios of weathered and parent rock samples, respectively.

Quantification of the overall mass transfer during weathering can be achieved by estimating the chemical component transfer, according to Brimhall et al. (1991). An open-system mass-fraction transport function was used to quantify the addition or subtraction of Ni and other elements during weathering.

$$\tau_{Ni,w} = \left(\frac{\rho_w \, . \, C_{Ni,w}}{\rho_p \, . C_{Ni,p}}\right) . \, (\epsilon_{Zr,w} + 1) - 1 \quad (3)$$

Where the subscripts p and w refer to the parent and weathered materials, respectively; ρ is bulk density in $g/cm^{3,}$ and C is the chemical concentration of any element in weight percent (wt%).

ϵ represents the volumetric strain, or volume change, corresponding to the relative difference of the product of density ρ and concentration C of an immobile element (in this case, Zr) in the weathered material compared to the parent rock as follows (Brimhall et al., 1991; Braun et al., 1993; Poitrasson et al., 2008):

$$\epsilon_{Zr,w} = \left(\frac{\rho_p \, .C_{Zr,p}}{\rho_w \, .C_{Zr,w}}\right) - 1 \qquad (4)$$

Positive, negative, or approximately zero values for $\epsilon_{Zr,w}$ indicate volume expansion, collapse, and isovolumetric weathering, respectively (Brimhall et al., 1991; Poitrasson et al., 2008). Finally, a positive value for $\tau_{Ni,\,w}$ reflects a true mass gain in nickel of the weathered sample compared to the parent rock, and negative values indicate a mass loss in the element. If $\tau_{Zr,\,w} = 0$, the element is immobile during weathering (Poitrasson et al., 2008).

Finally, the total mass of nickel (ΔM_{Ni}) transferred through the weathering system with thickness z cm, expressed in gNi cm^{-2}, is given by:

$$\Delta M_{Ni} = \left(100.\, \rho_p \, .\, C_{Ni,p}\right) . \int_{0}^{z} \tau_{Ni,w} \; .\, dz \qquad (5)$$

4. Results

4.1 The organization of the weathering profile

Based on the macroscopic observations and mineralogical and geochemical characteristics (see below), the SPC regolith profile (29 samples) is structured following major units: deep unweathered rock from around 200 m (Puma 28 and 29 samples), saprock from 45 m to 26.10 m (Puma 27 to Puma 21 samples), lower saprolite from 26.10 m to 17.15 m (Puma 20 to Puma 15 samples), upper saprolite corresponding to the depth ranging from 17.15 m to 3.5 m (Puma 14 to Puma 5 samples), and the limonite from 3.5 m to 0 m (Puma 4 to Puma 1 samples) (**Figure 2**).

Journal Pre-proof

4.2 . Mineralogy of the weathering profile

The rock samples consist mainly of intensely serpentinized pseudomorph pyroxene and olivine (**Figure 2G**). The olivine and pyroxene crystals show typical basal sections but are completely altered, which is related to peridotite serpentinization. Chromite, which is highly resistant to weathering processes (Garnier et al., 2008), occurring in all samples, is certainly the main chromium mineral. Locally, calcite-filled fractures and fibrous minerals, such as talc, have been interpreted as mineral crystallization in fractures during the serpentinization process. An association between bluish-green serpentine and chlorite is observed in these deeper samples, forming a fibrous matrix (> 90%) (**Figure 2F**). Chromite is fine-grained, euhedral to subhedral (< 10%). In the saprock and saprolite horizons, serpentine remains the dominant mineral and forms a dense matrix. In some saprock and saprolite sections, irregularly shaped and mesh-textured calcite veins cut through the serpentinized matrix (**Figure 2D and E**). A quartz botryoidal structure with a boundary composed of goethite associated with hematite is observed in the limonite samples and locally in deeper ferruginous saprolite zones (upper saprolite, **Figure 2C**). The greenish matrix observed in the deeper samples is gradually replaced by a reddish-orange matrix, most likely composed of Fe oxyhydroxides (**Figure 2B**), from the upper saprolite horizon.

The XRD analyses show that the serpentinite, saprock, and saprolite samples consist mainly of serpentine, chlorite, and chromite (**Figures 2 and S6**). The serpentine and chlorite are identified as chrysotile/lizardite and clinochlore/nimite, respectively, based on their characteristic peaks at 7.28 Å and 14.07 Å, respectively. Minor amounts of talc-like phases (peak at 9.15 Å) are observed in the XRD patterns of the saprock samples (Puma 26).

Iron and aluminum oxyhydroxides are the main minerals in the limonite samples. Goethite and hematite are identified with their characteristic peaks at 4.24 Å and 2.69 Å, respectively, and gibbsite is identified with a peak at 4.84 Å. Hematite typically occurs from the top of the saprock and the bottom of the lower saprolite horizons and becomes more dominant in the uppermost sections of the profile. In the upper saprolite and limonite, a well-defined peak at 3.34 Å reveals the occurrence of quartz in the uppermost horizon of the section. Smectite is not detected on limonite, even after ethylene glycol and heat treatments (**Figure S7**). However, a soft peak at 30 Å, mainly observed in limonite samples XRD patterns, suggests the occurrence of corrensite, an interstratified clay mineral that combines chlorite and smectite structures. Finally, peaks at 3.11 Å and 9.52 Å have been observed for the clay fraction in limonite samples, revealing the presence of pyrolusite and lithiophorite, both Mn oxides (**Figure S7**).

Journal Pre-proof

4.3 . Geochemical composition along the weathering profile

4.3.1 Major, minor, and trace elements

Figure 3 shows the geochemical distribution of the SPC profile. The serpentinite and saprock exhibit similar compositions (**Table 1 and Figure S1**). Serpentinite shows mean values of 12.86 ± 0.37 wt% Fe_2O_3, 40.0 ± 0.04 wt% MgO, 43.5 ± 0.3 wt% SiO_2, and 0.32 ± 0.02 wt% NiO; while saprock shows concentrations of 10.2 ± 2.0 wt% Fe_2O_3, 43.2 ± 2.3 wt% MgO, 43.3 ± 4.7 wt% SiO_2, and 0.4 ± 0.05 wt% NiO (**Figure 3A and B**).

From saprock to limonite, the profile is characterized by a progressive increase in Fe_2O_3 (3.2 to 75.7 wt%) and a decrease in MgO (50.0 to 2.0 wt%). SiO_2 remains relatively constant in the saprock and saprolite (43.7 ± 3.4 wt%), while it decreases from 46.5 wt% in the upper saprolite to 11.5 wt% in limonite samples. Iron enrichment is accompanied by aluminum enrichment and the presence of gibbsite in the limonite XRD patterns (**Figure 3A**).

The nickel concentrations in the saprock and lower saprolite are low (0.5 ± 0.2 wt% NiO). It increases in the upper saprolite (2.3 ± 0.4 wt%), reaching the highest concentration (3.0 wt%, Puma 5 sample). In the limonite, Ni concentration decreases to 1.0 ± 0.2 wt% (**Figure 3B)**.

Manganese and chromium behave similarly along the profile; the lowest concentrations are observed in serpentinite, saprock, and saprolite (0.27 ± 0.06 wt% MnO and 0.6 ± 0.2 wt% Cr_2O_3), while their concentrations increase in the range of 0.75–1.22 wt% MnO and 2.3–3.0 wt% Cr_2O_3 in limonite. The Mn concentrations in the limonite samples are approximately four times greater than those in the saprock unit. Accordingly, as observed in other Ni lateritic profiles (Gerth, 1990; Singh et al., 2002; Butt and Cluzel, 2013; Ulrich et al., 2019 and references therein), Mn oxides (lithiophorite and pyrolusite) may represent secondary Mn minerals in the SPC weathering profile (**Figure 3C)**. Al_2O_3 exhibits low concentrations along the profile, with strong enrichment in the limonite samples (0.25 wt% in saprock to 7.86 wt% in limonite samples) (**Figure 3B)**. The TiO_2 concentrations are relatively constant throughout the profile, with enrichment in the limonite samples (0.02 wt% in saprock to 0.53 wt% in limonite) with a mean value of 0.06 ± 0.02 wt% TiO_2 in saprock, lower saprolite, and upper saprolite (**Figure 3C)**.

Total Rare Earth Elements (ΣREE) range from 168 to 1,226 μg kg^{-1} in serpentinite, saprock, and saprolite, reaching up to 21,976 μg kg^{-1} in limonite (**Table S1 and Figure S8**). No Ce-positive anomaly are observed along the entire weathering profile (**Figure 3D**). Limonite shows fractionated REE chondrite-normalized patterns (Barrat et al., 2012), characterized by enrichment in Light Rare Earths Elements (LREE) over Heavy Rare Earths Elements (HREE) where saprolite and saprock are depleted in LREE compared to the chondrite (**Figure S8**).

Journal Pre-proof

4.3.2 Long-term nickel fluxes in the weathering profile

The saprock unit exhibits significant heterogeneity in texture and chemical composition (i.e., Fe_2O_3, MgO, TiO_2, and REE concentrations). Therefore, a composite sample with the average values of seven saprock samples (Puma 21 to Puma 27) is assumed to be a better reference for unaltered material in relation to the adjacent weathered samples. Therefore, the average values are used for the parameters (in Eqs. 2, 3, and 4) to quantify the mobility of the elements and their fluxes ($\tau_{Ni,\ w}$, EF_{Ni}, and ΔM_{Ni}).

The top of the upper saprolite corresponds to the largest Ni enrichment zone, reaching an EF_{Ni} average of 3.27 ± 0.7 against 0.26 ± 0.10 in limonite samples (**Figure 4A**). The quantification of mass loss ($\tau_{Ni,\ w}$) shows that Ni loss occurs for all limonite samples (i.e., negative $\tau_{Ni,\ w}$ values are computed). Contrastingly, upper and lower saprolite and saprock samples correspond to a net gain of Ni (positive $\tau_{Ni,\ w}$ values).

The overall or net mass flux ΔM_{Ni} shows the average loss of Ni in g per cm^2 of the weathering profile in the considered thickness (Brimhall et al., 1991). In the SPC profile, limonite samples show an average Ni loss of 0.53 ± 0.1 gNi cm^{-2}. Otherwise, the top of the upper saprolite shows the main mass gain zone with an average of 1.75 ± 0.4 gNi cm^{-2}. Sample Puma 5, at the top of the upper saprolite, shows the most significant gain calculated with 2.48 gNi cm^{-2} of Ni in a thickness of 1.15 m (**Table 1 and Figure 4B**).

4.3.3 Fraction of Ni associated with reducible Fe and Mn oxyhydroxides (DCB)

The results of DCB extraction (**Figure 5, and Table S3**) show that about 71% of Fe in the limonite samples are associated with oxyhydroxides, with an average of 364 ± 21 g kg^{-1}. Upper and lower saprolite concentrations reach an average of 52 ± 24 g kg^{-1} and 21 ± 8 g kg^{-1}, respectively (37% and 19% of total Fe). The saprock unit represents the smallest contribution to Fe in oxyhydroxides with a mean value of 12 ± 1 g kg^{-1}, corresponding to less than 15% of the total Fe (**Figure 5A**). Around 80% of the total Mn in the limonite samples is found in the DCB fraction with a mean value of 6.0± 0.5 g kg^{-1}. In the upper saprolite, it reaches a mean concentration of 1.3 ± 0.2 g kg^{-1}, representing 56% of the total Mn (**Figure 5B**).

Nickel extracted by DCB ranges from 2.0 ± 0.9 g kg^{-1} (10% of the total Ni) in the upper saprolite to 6.2 ± 1.1 g kg^{-1} (74% of the total Ni) in limonite (**Figure 5C**). Ni and Mn are not significantly associated with oxyhydroxides in the deeper zones of the profile, where the samples are less altered.

Journal Pre-proof

4.5. Nickel isotopic composition

The δ^{60}Ni values of the SPC profile samples range from -0.57 ± 0.07‰ (top of upper saprolite) to +0.52 ± 0.07‰ (bottom of lower saprolite) (**Table 1 and S2**). The δ^{60}Ni is positive in saprock and lower saprolite, with a mean of +0.25 ± 0.10 ‰, exhibiting samples enriched in heavy Ni isotopes such as Puma 20, 24, and 26. Overall, the enrichment of light Ni isotopes is observed from the lower saprolite to the top of the profile in the limonite samples (**Figure 6**).

The heaviest Ni isotope composition is found at the bottom of the saprolite, above the saprock samples (+0.52 ± 0.07‰). The saprock unit (n = 7) exhibits a mean δ^{60}Ni value of +0.26 ± 0.09‰. The δ^{60}Ni values of the lower saprolite unit vary from +0.42 ± 0.07‰ to +0.08 ± 0.07‰, with an average value of +0.22 ± 0.10 ‰ (n = 6). The upper saprolite unit is characterized by a light Ni isotopic signature, with an average value of –0.33 ± 0.17 ‰ (n = 10). The top of the upper saprolite (Puma 5) shows the lightest Ni isotopic signature with a mean δ^{60}Ni value of –0.57 ± 0.07‰. Finally, the limonite samples display light δ^{60}Ni and homogeneous isotopic signature, with an average value of –0.46 ± 0.03 ‰ (n = 4).

Hereafter, average Ni isotopic compositions were used to calculate the Δ^{60}Ni values. The fractionation factor between lower saprolite and saprock is Δ^{60}Ni = +0.02‰ while saprolite shows higher fractionation factors: $\Delta^{60}\text{Ni}_{\text{top of upper saprolite – lower saprolite}}$ = –0.40‰ and $\Delta^{60}\text{Ni}_{\text{upper saprolite top – bottom}}$ = –0.34‰. Finally, the fractionation factor between limonite and the top of upper saprolite is Δ^{60}Ni = +0.04‰.

5. Discussion

5.1 . Mineralogy and element distribution with depth

The mineralogical and geochemical results of the SPC laterite Ni-deposit revealed a deep protolith composed of almost completely serpentinized peridotite. Notably, primary ultramafic minerals such as olivine and pyroxene were not identified in the deepest serpentinite samples in the XRD analyses, but pyroxene and olivine pseudomorphs were observed in the thin sections of the serpentinized peridotite protolith samples.

From the saprock to the upper saprolite, serpentine is the dominant phase derived from the hydration of primary minerals; however, as the regolith becomes more developed, chlorite appears to be an important phase. In the upper saprolite unit, where major enrichment was observed, serpentine decreased and chlorite increased from the base to the top. In the XRD patterns, the serpentine peaks widen until they disappear in the limonite unit, where well-formed chlorite peaks are substituted.

Journal Pre-proof

Machado et al. (2021) suggested that part of the chlorite in the Santa Fé deposit (Brazil) is a supergene and can incorporate Ni into its structure, becoming an important single ore mineral in the regolith. According to Beaufort et al. (2015), primary chlorite commonly occurs in serpentinized dunite, whereas supergene chlorite may occur along the profile and is related to serpentine alteration. Previous studies have identified interstratified clinochlore throughout serpentine crystals (Cressey et al., 2008; Machado et al., 2021). However, the SPC limonite unit, which corresponds to a chlorite-rich zone, did not exhibit significant Ni enrichment.

Major elements (SiO_2, MgO, and Fe_2O_3) showed almost constant behavior throughout the saprock, lower saprolite, and upper saprolite horizons until a transition zone marked by a Mg discontinuity (from 35.7 ± 3.2 wt% to 3.4 ± 1.7 wt%, MgO) (**Figure 3**). Serpentine was no longer observed, and residual Fe was concentrated in the uppermost zone, reaching 72.9 ± 1.4 wt% (Fe_2O_3), forming Fe oxyhydroxides. The transition zone, characterized by Mg and Fe discontinuities, is typical of serpentinic weathering profiles (Butt and Cluzel, 2013). In SPC, the discontinuity is abrupt. This feature led to the hypothesis that the studied SPC weathering profile comprises both autochthonous and allochthonous sections. In this case, the regolith profile is truncated, and the limonite unit represents a mature, altered, and allochthonous material deposited over an eroded profile. However, the Puma weathering profile is similar to that of the Loma Peguera ore deposit (Falcando, Dominican Republic) (Aiglsperger et al., 2016), with a similar abrupt transition at the top of the regolith.

The chemical heterogeneity observed in the saprolite unit, with layers richer in Fe than the others, suggests that weathering occurred heterogeneously towards the profile. The more weathered zones (e.g., Puma 10) that occur in deeper horizons may be related to fractures. This feature may highlight the supergenic alteration associated with preferential meteoric water percolation in fractured zones. Hematite appeared in the lower saprolite and became the main mineral phase in limonite. Moreover, in deeper horizons, the most iron-enriched samples coincided with high crystallinity hematite in the XRD analysis (i.e., Puma 10). In limonite, the Fe concentration reached approximately 75 wt% Fe_2O_3, hematite peaks become less wide and much more intense, and goethite peaks appear (**Figure S6**).

The Mn oxides are significant Ni-host mineral phases in serpentine weathering profiles (Manceau et al., 1992; Quantin et al., 2002 ; Aiglsperger et al., 2016; Ulrich et al., 2019). Futhermore, in the case of δ^{60}Ni, Ni isotopic fractionation accompanies the incorporation of Ni in Mn oxy-hydroxides up to 3–4 times higher than the ones observed with clay minerals and Fe oxides (Gueguen et al., 2018). Therefore, even if Mn is present in very low amounts in the regolith, the Mn distribution is crucial for understanding Ni and Ni isotope behaviors during weathering. Previous

Journal Pre-proof

studies on weathering profiles have demonstrated a close link between REEs (Ce-positive anomalies) and Mn enrichment (Braun et al., 1990; Aiglsperger et al., 2016; Ulrich et al., 2019). Thus, the Ce distribution can trace the Mn oxides and their implications for Ni isotopic fractionation.

Even in the most weathered horizons of the SPC profile where occur REE enrichment, no Ce anomaly was observed (**Figure S8**). This absence of Ce anomalies can be related to lower Mn concentrations and lower Mn oxide contributions compared to other studied profiles, with an average of 0.98 ± 0.1 against 4.9 ± wt% MnO in the Loma Caribe profile (Republic Dominican, Aiglsperger et al., 2016). Considering the low Mn concentration and the lack of Mn oxide-rich zones in the SPC profile, the Ni isotope fractionations observed along the entire profile were mainly assigned to Ni interactions with clay minerals and iron oxides (adsorption and co-precipitation processes).

5.1.1 Nickel distribution

The Ni concentration gradually increases from the saprock to the upper saprolite, reaching its highest value (3.10 wt% NiO, sample Puma 5). The concentrations decreased significantly above the upper saprolite layer in the limonite samples (**Figure 3**). Negative $\tau_{Ni,\ w}$ values for all the limonite samples confirmed that this horizon represents a leached zone with an average Ni loss of 0.53 ± 0.1 g $cm^{-2,}$ and part of the leached Ni appears to be retained mainly in the top of the upper saprolite where the mass gain reached 1.75 ± 0.4 g cm^{-2} (**Figure 4C**). It is likely that during weathering, parts of the Mg, Si, and Ni were leached from the surface horizons and partly retained in the secondary serpentines in the upper saprolite. This feature was emphasized at the top of the upper saprolite, where the EF_{Ni} was up to three times higher than that of the saprock (**Figure 4A**).

At the very top of the weathering profile, Ni was mainly hosted by hematite and goethite, as 74.6% of the total Ni in the limonite was solubilized during the DCB extraction (**Figure 5**). This is similar to what was described for the New Caledonia deposits (where the sum of hematite and goethite represent 75% of the Ni contribution in ferruginous zones, Ulrich et al., 2019). XRD analyses performed on the sample residue after DCB extraction showed that in addition to chlorite and chromite, hematite may have withstood the DCB procedure, even though the concentrations of metals in this fraction were relatively high (**Figure S7**).

Finally, as expected, the low Ni-DCB concentration in the deeper samples (i.e., upper and lower saprolite) suggests that the silicate phases host Ni in these horizons, which are likely composed of serpentine and chlorite. Talc-like minerals did not seem to be an important Ni ore mineral in the SPC Ni-deposit because they were only described in one sample in the saprock unit.

Journal Pre-proof

Journal Pre-proof

5.2 Nickel isotopes distribution in lateritic systems

Serpentinite samples in the SPC profile showed a Ni isotopic signature of 0.24–0.26 ± 0.07 ‰ (Puma 28 and 29, respectively). These values are similar for saprock and serpentinized rocks reported by previous works (Estrade et al., 2015; Ratié et al., 2018; Pędziwiatr et al., 2018) and in the interval of the Bulk Silicate Earth (BSE) data published by Gall et al. (2017) at δ^{60}Ni = 0.23 ± 0.08 ‰ and more recently by Klaver et al. (2019) and Wang et al. (2021) with 0.115 ± 0.011 ‰ and 0.10 ± 0.07 ‰, respectively. This dataset confirmed that serpentinization processes were not accompanied by significant isotopic fractionation relative to the BSE (Ratié et al., 2018). In contrast, high variability of δ^{60}Ni was observed in the regolith from –0.57 ± 0.07 ‰ to 0.52 ± 0.07 ‰. Moreover, isotopically heavier Ni dissolved and leached during weathering processes can be mobilized downwards and lost from the profile. They can be incorporated into secondary minerals that form in the weathering profiles (Ratié et al., 2018). In agreement, the SPC profile showed the heaviest Ni isotopic signature in the lower saprolite horizon (δ^{60}Ni = 0.52 ± 0.07‰, **Figure 6**).

Compared with the BSE signature, samples of the SPC profile became enriched in light Ni isotopes towards the top, particularly in the limonite and upper saprolite samples. These results are similar to those obtained from lateritic profiles (Gleeson et al., 2004; Ratié et al., 2015; 2018) and soil developed from serpentinite in the Mediterranean (Estrade et al., 2015) and temperate climates (Pędziwiatr et al., 2018; Spivak-Birndorf et al., 2018). Heavier isotope depletion was observed in the solid phase during the weathering with $\Delta^{60}\mathrm{Ni}_{\mathrm{limonite\,-\,Saprock}}$ = –0.72‰. The SPC weathering profile showed lighter values than those reported by Ratié et al. (2015) in the Barro Alto Ni-deposit ($\Delta^{60}\mathrm{Ni}_{\mathrm{limonite\,-\,Saprock}}$ = –0.47‰). The lightest δ^{60}Ni values correspond to the highest amounts of Ni associated with Fe oxyhydroxides (DCB extractions). This is in agreement with the preferential adsorption of light Ni isotopes (Wasylenki et al., 2015; Wang and Wasylenki, 2017; Gueguen et al., 2018) on the surface because Ni has a more stable coordination geometry in the solid phase than in the dissolved phase (Schauble, 2004; Fujii et al., 2014). The increased proportion of hematite in SPC limonite can lead to changes in Ni speciation and consequently, Ni isotopic fractionation (arrow 2, limonitization, **Figure 7**). Hematite and goethite have different Fe structures, with a larger number of Fe atoms in the second coordination shell in hematite than in goethite (Arai, 2008; Flynn and Catalano, 2019). The number of Fe atoms in the second shell was critical for Ni isotope fractionation (Gueguen et al., 2018). Therefore, the magnitude of Ni isotope fractionation during Ni adsorption onto hematite should be smaller than that on goethite. This may explain why the Ni isotopes in the limonitic unit were less fractionated than those in the upper saprolite. However, further research is needed to investigate the fractionation of Ni isotopes between the goethite and hematite solid phases.

Journal Pre-proof

Nickel isotope measurements coupled with Ni mass balance shed light on Ni mobility in lateritic systems (**Figure 7**). As discussed earlier, limonite and upper saprolite samples are preferentially enriched in light Ni isotopes relative to saprock, and lower saprolite samples display a slight positive δ^{60}Ni value compared to the saprock isotopic signature. Both features reflect the redistribution of Ni isotopes during weathering. The biplot correlation between ΔM_{Ni} and δ^{60}Ni data in **Figure 7** emphasizes the Ni redistribution.

The saprolitization and limonitization could explain the evolution of the studied profile and the current setting. The lower saprolite displays a narrow isotopic change compared to the saprock ($\Delta^{60}Ni_{\text{lower saprolite – saprock}}$ = +0.02‰). In comparison, a significant δ^{60}Ni signature variation is recorded between the lower saprolite and the bottom of the upper saprolite. ($\Delta^{60}Ni_{\text{top of upper saprolite – lower saprolite}}$ = –0.40‰) (**Figure 7**, arrow 1a – incipient saprolitization). At this stage, Ni fractionation associated with gradual serpentine–chlorite transformations was accompanied by a slight Ni mass gain. The isotopic fractionation recorded from the bottom to the top of the upper saprolite is also large ($\Delta^{60}Ni_{\text{upper saprolite top – bottom}}$ = –0.34‰) (arrow 1b - saprolitization). Significant and continuous isotopic fractionation accompanied a large net Ni mass gain.

Toward the top of the profile, the transition between the upper saprolite and limonite is marked by the abrupt disappearance of serpentine and an increase in chlorite and Fe oxyhydroxides. The almost vertical arrow 2 (**Figure 7**), emphasizes that the limonitization is marked by a Ni loss without significant Ni isotopic fractionation ($\Delta^{60}Ni_{\text{limonite – top of upper saprolite}}$ = +0.04‰).

Finally, the results of this study show large Ni fractionation and gains in the overall weathered profile, and consequently, significant Ni fluxes in that Ni-deposit. Although a large Ni gain was observed at the weathered profile scale, the overall enrichment in light Ni isotopes involved the leaching of heavy Ni isotopes from the upper part. The two samples with heavy isotopic compositions combined with significant Ni gain (gray circle) highlight that part of the Ni heavy isotope leached from the top of the profile was likely retained in the lower saprolite, as already observed by Gall et al. (2013) for Cerra Motoso.

5.3. Implication for the Ni cycle at regional and global scales

The detailed insights into Ni isotopes in the Puma deposit of Carajas, coupled with chemical and mineralogical compositions, allow presenting for the first time Ni mass and isotopic balances on an entire weathering profile in the Amazonian Basin, which contributes to almost 20% of the world's freshwater to the ocean (Dai and Trenberth, 2002).

The isotopic mass balance (**Eq. 6**) is calculated for a weathering integration on a unit surface (1 cm²) based on the ΔM_{Ni} (g cm^{-2}) value calculated for each, i.e., depth thickness (sample Puma 1 to Puma 20, from the top to the base of the saprolite section) over 26.1 m (z_{tot}) to obtain the integrated $\delta^{60}Ni_{released}$ over the overall weathering in the ultramafic area of the SPC (**Eq. 7**).

$$\delta^{60}Ni_{unweathered\,profile} \times mNi_{unweathered\,profile} = \delta^{60}Ni_{released} \times mNi_{released} + \delta^{60}Ni_{weathered\,profile} \times mNi_{weathered\,profile} \quad \textbf{(6)}$$

$$\delta^{60}Ni_{released} = \left((\delta^{60}Ni_{protolith} \times [Ni]_{protolith} \times \rho_{protolith} \times z_{tot}) - (\frac{1}{n \times z_{tot}} \sum_{i=1}^{n} \delta^{60}Ni \times dz) \times mNi_{weathered\,profile} \right) / \sum_{i=1}^{n} \Delta M_{Ni} \quad \textbf{(7)}$$

Where n = 20 represents the 20 horizons from Puma 1 to Puma 20 with specific thickness (dz). The amount of Ni remaining in the weathered profile ($mNi_{weathered\ profile}$) was calculated as the difference between the initial mass of Ni in the profile ($mNi_{unweathered\ profile}$) and its loss after weathering ($mNi_{released}$). The $\delta^{60}Ni_{unweathered\ profile}$ has been attributed to the $\delta^{60}Ni_{protolith}$ value, 0.26 ± 0.11 ‰ (SD), calculated as the mean isotopic value from the rock samples (Puma 21 to Puma 29). The $\delta^{60}Ni_{weathered\ profile}$ has been defined as the mean isotopic value of the weathered profile from Puma 1 to Puma 20: –0.15 ± 0.32 ‰ (SD). For 1 cm², the $mNi_{unweathered\ profile}$ has been calculated at 18.2 g, and the $mNi_{released}$ has been described as the sum of the ΔM_{Ni} of each sample, 14.6 g (Supplementary Information).

The isotopic Ni mass balance allowed to determine the total isotopic Ni flux released during the weathering process of laterization in the SPC. This value of 0.36 ‰ ± 0.43 ‰ (SD) represents the average Ni isotopic signature of the total Ni released during several million years. The apparent heavy δ^{60}Ni leaching and loss observed in the SPC weathering profiles were consistent with published river and ocean isotopic datasets (Cameron and Vance, 2014; Revels et al., 2021). This calculated value cannot be directly linked to the current Ni isotopic composition measured in two main Amazonian river tributaries (the Rio Negro and Solimões) ranging from 0.31 to 0.88% (Cameron and Vance, 2014) or in the Amazon itself with δ^{60}Niv= +1.38‰ (Revels et al., 2021), which are not timescale dependent of the overall weathering stages. Moreover, this Ni isotopic flux was clearly modified from continent to ocean, as shown by the variable sequestration of light Ni secondary particulate phases, likely Fe oxyhydroxides (Revels, 2021), contributing to a probable heavier Ni isotopic dissolved flux coming from rivers and entering the ocean.

Journal Pre-proof

6. Conclusions

The weathering process of the SPC leads to a large redistribution of Ni along the profile and its residual accumulation in the weathered material. Serpentine and chlorite are the main Ni carriers in the upper saprolite horizon of the SPC weathering profile, reaching a concentration of 3.1 wt% NiO. Fe oxyhydroxides represent the main Ni-bearing phase in the limonite unit, which carries about 74.6% of the total Ni. The NiO concentration reaches 1.4 wt% in the limonite, although Ni loss was recorded in this zone. Otherwise, the SPC weathering profile exhibited a net gain of Ni. The negative $\tau_{Ni,\ w}$ values for all limonite samples confirmed that this horizon represents a leached zone, and part of the Ni leached appears to be retained mainly in the top of the upper saprolite, where the mass gain reached 1.75 ± 0.4 g cm^{-2}.

As observed in other laterite Ni-deposits, the overall Ni gain was associated with strong Ni isotopic fractionation. The overall SPC Ni isotopic profile confirms the preferential enrichment of light Ni isotopes in the solid phase relative to the parent rock during weathering. This observation is attributed to, (i) the incorporation of Ni in secondary chlorite and (ii) the adsorption of Ni on secondary minerals, such as Fe oxyhydroxides. In SPC, major isotopic fractionation was notably recorded during saprolitization, where serpentine–chlorite transformations may occur. The small Ni isotopic fractionation during limonitization has been attributed to Fe speciation changes, that is, the transformation of goethite into hematite

Finally, the SPC weathered profile exhibited a Δ^{60}Ni limonite-saprock of −0.72‰ resulting from intense weathering of serpentinite. The significant Ni gain combined with the light Ni isotopic signature in the upper saprolite and limonite led to the formation of a substantial light Ni isotope reservoir. As observed in previous studies, heavier Ni isotopes leached during weathering processes were partly incorporated into secondary minerals at the bottom of the profile. Moreover, the Ni mass balance model combined with isotopic compositions indicated that the Ni loss from the weathered serpentinite profile was isotopically heavy. The proposed Ni isotopic mass balance confirms the existence of a light Ni isotope reservoir on continents and that a large amount of heavy Ni isotopes is removed during weathering. The approach adopted in this study shows that the total Ni flux released during the weathering process is isotopically heavy, in agreement with the dissolved loads of Amazonian rivers and oceans.

Journal Pre-proof

Acknowledgments

This study was financed by the Coordenação de Aperfeiçoamento de Pessoal de Nível Superior – Brasil (CAPES) – Finance Code 001. The authors acknowledge the VALE-SA, professors, and technicians of the Geosciences Institute of Brasilia University (UnB) for the logistic and their assistance in the field. Analytical work at of UnB, GeoSciences Paris Saclay (GEOPS), Centre de Recherches Pétrographiques et Géochimiques (CRPG) - Nancy and HydroSciences Montpellier (HSM) was partly funded by the CNPq universal 445423/2014-5. JG was supported by CNPq grant 310750/2014-8 and 302722/2018-1. G. Ratié acknowledges the Labex VOLTAIRE, France (10-LABX-0100). We would like to express our gratitude to the reviewers, particularly Bleuenn Guéguen, for their dedicated time and effort in reviewing the manuscript. We sincerely appreciate all the valuable comments and suggestions provided, as they have significantly contributed to enhancing the quality of the manuscript.

Journal Pre-proof

REFERENCES

Aiglsperger, T., Proenza, J.A., Lewis, J.F., Labrador, M., Svojtka, M., Rojas-Purón, A., Longo, F., Ďurišová, J., 2016. Critical metals (REE, Sc, PGE) in Ni laterites from Cuba and the Dominican Republic. Ore Geol. Rev. 73, 127–147. https://doi.org/10.1016/j.oregeorev.2015.10.010

Aquino, K.A., Arcilla, C.A., Schardt, C., Tupaz, C.A.J., 2022. Mineralogical and Geochemical Characterization of the Sta. Cruz Nickel Laterite Deposit, Zambales, Philippines. Minerals 12. https://doi.org/10.3390/min12030305

Arai, Y., 2008. Spectroscopic evidence for Ni(II) surface speciation at the iron oxyhydroxides-water interface. Environ. Sci. Technol. 42, 1151–1156. https://doi.org/10.1021/es0719529

Araújo, O.D., Maia, R.G.N., João, X.D.S.J., Costa, J.B.S., 1988. A megaestruturação arqueana da folha Serra dos Carajás, in: Anais VII Congresso Latino Americano de Geologia, Belem. pp. 324–338.

Araujo, O.J.B., Maia, R.G.N., 1991. Serra dos Carajás Folha SB.22-Z-A - Estado do Pará.

Aquino, K.A., Arcilla, C.A., Schardt, C., Tupaz, C.A.J., 2022. Mineralogical and Geochemical Characterization of the Sta. Cruz Nickel Laterite Deposit, Zambales, Philippines. Minerals 12. https://doi.org/10.3390/min12030305

Barrat, J.A., Bayon, G., Lalonde, S., 2023. Calculation of cerium and lanthanum anomalies in geological and environmental samples. Chem. Geol. 615, 121202. https://doi.org/10.1016/j.chemgeo.2022.121202

Barrat, J.A., Zanda, B., Moynier, F., Bollinger, C., Liorzou, C., Bayon, G., 2012. Geochemistry of CI chondrites: Major and trace elements, and Cu and Zn Isotopes. Geochim. Cosmochim. Acta 83. https://doi.org/10.1016/j.gca.2011.12.011

Beaufort, D., Rigault, C., Billon, S., Billault, V., Inoue, A., Inoue, S., Patrier, P., 2015. Chlorite and chloritization processes through mixed-layer mineral series in low-temperature geological systems – a review. Clay Miner. 50, 497–523. https://doi.org/10.1180/claymin.2015.050.4.06

Berger, A., Frei, R., 2014. The fate of chromium during tropical weathering: A laterite profile from central Madagascar. Geoderma 213, 521–532. https://doi.org/10.1016/j.geoderma.2013.09.004

Brand, N.W., Butt, C.R.M., Elias, M., 1998. Nickel laterites: classification and features. AGSO J. Aust. Geol. Geophys. 17, 81–88.

Braun, J.J., Pagel, M., Herbilln, A., Rosin, C., 1993. Mobilization and redistribution of REEs and thorium in a syenitic lateritic profile: A mass balance study. Geochim. Cosmochim. Acta 57, 4419–4434. https://doi.org/10.1016/0016-7037(93)90492-F

Journal Pre-proof

Braun, J.J., Pagel, M., Muller, J.P., Bilong, P., Michard, A., Guillet, B., 1990. Cerium anomalies in lateritic profiles. Geochim. Cosmochim. Acta 54, 781–795. https://doi.org/10.1016/0016-7037(90)90373-S

Brimhall, G.H., Christopher J., L., Ford, C., Bratt, J., Taylor, G., Warin, O., 1991. Quantitative geochemical approach to pedogenesis: importance of parent material reduction, volumetric expansion, and eolian influx in lateritization. Geoderma 51, 51–91. https://doi.org/10.1016/0016-7061(91)90066-3

Butt, C.R.M., Cluzel, D., 2013. Nickel laterite ore deposits: Weathered serpentinites. Elements 9, 123–128. https://doi.org/10.2113/gselements.9.2.123

Cameron, V., Vance, D., 2014. Heavy nickel isotope compositions in rivers and the oceans. Geochim. Cosmochim. Acta 128, 195–211. https://doi.org/10.1016/j.gca.2013.12.007

Cameron, V., Vance, D., Archer, C., House, C.H., 2009. A biomarker based on the stable isotopes of nickel. Proc. Natl. Acad. Sci. U. S. A. 106, 10944–10948. https://doi.org/10.1073/pnas.0900726106

Colin, F., Nahon, D., Trescases, J.J., Melfi, J., 1990. Lateritic weathering of pyroxenites at Niquelândia, Goiás, Brazil: The supergene behavior of nickel. Econ. Geol. 85, 1010–1023.

Cressey, G., Cressey, B.A., Wicks, F.J., 2008. The significance of the aluminium content of a lizardite at the nanoscale: the role of clinochlore as an aluminium sink. Mineral. Mag. 72, 817–825. https://doi.org/10.1180/minmag.2008.072.3.817

Dai, A.; Trenberth, K.E., 2002. Estimates of Freshwater Discharge from Continents: Latitudinal and Seasonal Variations. *J. Hydrometeorol.*, *3*, 660–687. https://doi.org/10.1175/1525-7541(2002)003<0660:EOFDFC>2.0.CO;2

Domènech, C., Villanova-de-Benavent, C., Proenza, J.A., Tauler, E., Lara, L., Galí, S., Soler, J.M., Campeny, M., Ibañez-Insa, J., 2022. Co–Mn Mineralisations in the Ni Laterite Deposits of Loma Caribe (Dominican Republic) and Loma de Hierro (Venezuela). Minerals 12, 927. https://doi.org/10.3390/min12080927

Dublet, G., Juillot, F., Morin, G., Fritsch, E., Fandeur, D., Ona-Nguema, G., and Brown, G.E. (2012). Ni speciation in a New Caledonian lateritic regolith: A quantitative X-ray absorption spectroscopy investigation. Geochim. Cosmochim. Acta *95*, 119–133. https://doi.org/10.1016/j.gca.2012.07.030

Elias, M., 2002. Nickel laterite deposits – geological overview, resources and exploitation. Cent. Ore Depos. Res. Univ. Tasmania, Hobart, Spec. Publ. 4, 205–220.

Estrade, N., Cloquet, C., Echevarria, G., Sterckeman, T., Deng, T., Tang, Y., Morel, J. L. (2015). Weathering and vegetation controls on nickel isotope fractionation in surface ultramafic environments (Albania). *Earth and Planetary Science Letters*, *423*, 24-35. https://doi.org/10.1016/j.epsl.2015.04.018Get rights and content

Fan, R., Gerson, A.R., 2015. Synchrotron micro-spectroscopic examination of Indonesian nickel laterites. Am. Mineral. 100, 926–934. https://doi.org/10.2138/am-2015-5093

Feio, G.R.L., Dall’Agnol, R., Dantas, E.L., Macambira, M.J.B., Santos, J.O.S., Althoff, F.J., Soares, J.E.B., 2013. Archean granitoid magmatism in the Canaã dos Carajás area: Implications for crustal evolution of the Carajás province, Amazonian craton, Brazil. Precambrian Res. 227, 157–185. https://doi.org/10.1016/j.precamres.2012.04.007

Ferreira Filho, C.F., Cançado, F., Correa, C., Macambira, E.M.B., Siepierski, L., Junqueira-Brod, T.C., 2007. Mineralizações estratiformes de EGP-Ni associadas a complexos acamadados em Carajás: os exemplos de Luanga e Serra da Onça. Contrib. à Geol. da Amaz. 1–14.

Flynn, E.D., Catalano, J.G., 2019. Reductive transformations of layered manganese oxides by small organic acids and the fate of trace metals. Geochim. Cosmochim. Acta 250, 149–172. https://doi.org/10.1016/j.gca.2019.02.006

Freyssinet, P., Butt, C.R.M., Morris, R.C., Piantone, P., 2005. Ore-forming processes related to lateritic weathering. Econ. Geol. 100 Anniv, 681–722.

Fu, W., Yang, J., Yang, M., Pang, B., Liu, X., Niu, H., Huang, X., 2014. Mineralogical and geochemical characteristics of a serpentinite-derived laterite profile from East Sulawesi, Indonesia: Implications for the lateritization process and Ni supergene enrichment in the tropical rainforest. J. Asian Earth Sci. 93, 74–88. https://doi.org/10.1016/j.jseaes.2014.06.030

Fujii, T., Moynier, F., Blichert-Toft, J., Albarède, F., 2014. Density functional theory estimation of isotope fractionation of Fe, Ni, Cu, and Zn among species relevant to geochemical and biological environments. Geochim. Cosmochim. Acta 140, 553–576. https://doi.org/10.1016/j.gca.2014.05.051

Gall, L., Williams, H.M., Halliday, A.N., Kerr, A.C., 2017. Nickel isotopic composition of the mantle. Geochim. Cosmochim. Acta 199, 196–209. https://doi.org/10.1016/j.gca.2016.11.016Get rights and content

Gall, L., Williams, H.M., Siebert, C., Halliday, A.N., Herrington, R.J., Hein, J.R., 2013. Nickel isotopic compositions of ferromanganese crusts and the constancy of deep ocean inputs and continental weathering effects over the Cenozoic. Earth Planet. Sci. Lett. 375, 148–155. https://doi.org/10.1016/j.epsl.2013.05.019

Garnier, J., Quantin, C., Guimarães, E., Becquer, T., 2008. Can chromite weathering be a source of Cr in soils? Mineral. Mag. 72, 49–53. https://doi.org/10.1180/minmag.2008.072.1.49

Gerth, J., 1990. Unit-cell dimensions of pure and trace metal-associated goethites. Geochim.

Journal Pre-proof

Cosmochim. Acta 54, 363–371. https://doi.org/10.1016/0016-7037(90)90325-F

Gleeson, S.A., Herrington, R.J., Durango, J., Velásquez, C.A., Koll, G., 2004. The mineralogy and geochemistry of the Cerro Matoso S.A. Ni Laterite deposit, Montelíbano, Colombia. Econ. Geol. 99, 1197–1213. https://doi.org/10.2113/gsecongeo.99.6.1197

Golightly, J.P., 2010. Progress in Understanding the Evolution of Nickel Laterites. Chall. Find. New Miner. Resour. Metallog. Innov. Explor. New Discov. 1–26. https://doi.org/10.5382/SP.15.2.07

Gueguen, B., Sorensen, J. V., Lalonde, S. V., Peña, J., Toner, B.M., Rouxel, O., 2018. Variable Ni isotope fractionation between Fe-oxyhydroxides and implications for the use of Ni isotopes as geochemical tracers. Chem. Geol. 481, 38–52. https://doi.org/10.1016/j.chemgeo.2018.01.023

Gueguen, B., Rouxel, O., Ponzevera, E., Bekker, A., Fouquet, Y., 2013. Nickel isotope variations in terrestrial silicate rocks and geological reference materials measured by MC-ICP-MS. Geostand. Geoanalytical Res. 37, 297–317 https://doi.org/10.1111/j.1751-908X.2013.00209.x

Klaver, M., Ionov, D. A., Takazawa, E., Elliott, T. (2019). The non-chondritic Ni isotope composition of Earth’s mantle. *Geochimica et Cosmochimica Acta*, *268*, 405-421. https://doi.org/10.1016/j.gca.2019.10.017

Komárek, M., Ratié, G., Vaňková, Z., Šípková, A., Chrastný, V., 2022. Metal isotope complexation with environmentally relevant surfaces: opening the isotope fractionation black box. Critical Reviews in Environmental Science and Technology 52, 3573–3603.

Macambira, E.M.B., 1997. Geologia e aspectos metalogenéticos dos elementos do Grupo da Platina no Complexo Máfico-Ultramáfico da Serra da Onça - sul do Pará. Universidade Federal do Pará.

Macambira, E.M.B., Ferreira Filho, C.F., 2002. Fracionamento Magmático dos Corpos Máfico-Ultramáficos da Suíte Intrusiva Cateté – Sul do Pará, in: Klein, E.L., Vasquez, M.L., Rosa Costa, L.T. (Eds.), Contribuições à Geologia Da Amazônia. SBG-Núcleo Norte, pp. 105–114.

Macambira, E.M.B., Vale, G., 1997. Programa Levantamentos Geológicos Básicos do Brasil. São Felix do Xingu. Folha SB.22-Y-B. Estado do Pará.

Machado, M.L., Porto, C.G., Santoro, L., Putzolu, F., Neumann, R., Bastos Neto, A., Polivanov, H., Herrington, R., 2021. The origin of supergene nickeliferous chlorite in the Santa Fé Ni-Laterite Deposit, GO, Brazil. Brazilian J. Geol. 51. https://doi.org/10.1590/2317-4889202120200119

Manceau, A.I. Gorshkov, V.A. Drits, 1992. Structural chemistry of Mn, Fe, Co, and Ni in Mn hydrous oxides. II. Information from EXAFS spectroscopy, electron and X-ray diffraction Am. Mineral., 77, 1144-1157

Mansur, E.T., Ferreira Filho, C.F., Oliveira, D.P.L., 2016. The Luanga deposit, Carajás Mineral

Journal Pre-proof

Province, Brazil: Different styles of PGE mineralization hosted in a medium-size layered intrusion. Ore Geol. Rev. 118. https://doi.org/10.1016/j.oregeorev.2020.103340

Mehra, O.P., Jackson, M.L., 1960. Iron Oxide Removal From Soils and Clays By a Dithionite–Citrate System Buffered With Sodium Bicarbonate. Clays Clay Miner. 317–327. https://doi.org/10.1016/B978-0-08-009235-5.50026-7

Merrot, P ; Juillot, F.; Flipo, L. ; Tharaud, M. ; Viollier, E. ; Noël, V. ; Le Pape, P. ; Fernandez, J-M.; Moreton, B.; Morin, G. 2022. Bioavailability of chromium, nickel, iron and manganese in relation to their speciation in coastal sediments downstream of ultramafic catchments: A case study in New Caledonia. Chemosphere, https://doi.org/10.1016/j.chemosphere.2022.134643

Moynier, F., Blichert-Toft, J., Telouk, P., Luck, J.M., Albarède, F., 2007. Comparative stable isotope geochemistry of Ni, Cu, Zn, and Fe in chondrites and iron meteorites. Geochim. Cosmochim. Acta 71, 4365–4379. https://doi.org/10.1016/j.gca.2007.06.049

Nesbitt, H.W., Wilson, R.E., 1992. Recent chemical weathering of basalts. Am. J. Sci. 833 292, 740–777. https://doi.org/10.2475/ajs.292.10.740

Neubeck, A., Hemmingsson, C., Boosman, A., Rouxel, O., Bohlin, M., 2021. Ni isotope fractionation during coprecipitation of Fe(III)(oxyhydr)oxides in Si solutions. Geochemistry 81, 125714. https://doi.org/10.1016/j.chemer.2020.125714

Noël, V., Juillot, F., Morin, G., Marchand, C., Ona-Nguema, G., Viollier, E., Prevot, F., Dublet, G., Maillot, F., Delbes, L., Marakovic, G., Bargar, J.R., Brown Jr., G.E., 2017. Oxidation of Ni-rich mangrove sediments after isolation from the sea (Dumbea Bay, New Caledonia): Fe and Ni behavior and environmental implications. ACS Earth and Space Chemistry. https://doi.org/10.1021/acsearthspacechem.7b00005.

Pędziwiatr, A., Kierczak, J., Waroszewski, J., Ratié, G., Quantin, C., Ponzevera, E., 2018. Rock-type control of Ni, Cr, and Co phytoavailability in ultramafic soils. Plant Soil 423, 339–362. https://doi.org/10.1007/s11104-017-3523-3

Poitrasson, F., Viers, J., Martin, F., Braun, J.J., 2008. Limited iron isotope variations in recent lateritic soils from Nsimi, Cameroon: Implications for the global Fe geochemical cycle. Chem. Geol. 253, 54–63. https://doi.org/10.1016/j.chemgeo.2008.04.011

Quantin, C., Becquer, T., Berthelin, J., 2002. Les oxydes de Mn: Une source majeure de Co et Ni facilement mobilisables en conditions réductrices dans les Ferralsols de Nouvelle-Calédonie. Comptes Rendus Geosci. 334, 273–278. https://doi.org/10.1016/S1631-0713(02)01753-4

Rasti, S., rajabzadeh, M. A., Monvoisin, G., Quantin, C. 2022. Investigation of the Ni-rich regolith in Bavanat region, Fars province, Iran: Constraints from mineralogy, geochemistry and Ni isotopes. J. of Geochem Exploration, 242, 107086.

Journal Pre-proof

https://doi.org/10.1016/j.gexplo.2022.107086

Ratié, G., Garnier, J., Calmels, D., Vantelon, D., Guimarães, E., Monvoisin, G., Nouet, J., Ponzevera, E., Quantin, C., 2018. Nickel distribution and isotopic fractionation in a Brazilian lateritic regolith: Coupling Ni isotopes and Ni K-edge XANES. Geochim. Cosmochim. Acta 230, 137–154. https://doi.org/10.1016/j.gca.2018.03.026

Ratié, G., Jouvin, D., Garnier, J., Rouxel, O., Miska, S., Guimarães, E., Cruz Vieira, L., Sivry, Y., Zelano, I., Montarges-Pelletier, E., Thil, F., Quantin, C., 2015. Nickel isotope fractionation during tropical weathering of ultramafic rocks. Chem. Geol. 402, 68–76. https://doi.org/10.1016/j.chemgeo.2015.02.039

Revels, B. N., Rickli, J., Moura, C. A., Vance, D. (2021). Nickel and its isotopes in the Amazon Basin: The impact of the weathering regime and delivery to the oceans. *Geochimica et Cosmochimica Acta, 293*, 344-364. https://doi.org/10.1016/j.gca.2020.11.005

Rosa, W.D., 2014. Complexos acamadados da Serra da Onça e Serra do Puma: Geologia e petrologia de duas intrusões Máfico-Ultramáficas com sequência de cristalização distinta na Província Arqueana de Carajás, Brasil. Universidade de Brasília.

Schauble, E., Rossman, G.R., Taylor, H.P., 2004. Theoretical estimates of equilibrium chromium-isotope fractionations. Chem. Geol. 205, 99–114 https://doi.org/10.1016/j.chemgeo.2003.12.015

Silva, M.L.M. de C., Oliveira, S.M.B. de, 1995. As Fases Portadoras De Níquel Do Minério Laterítico De Níquel Do Vermelho, Serra Dos Carajás (Pa). Rev. Bras. Geociências 25, 69–78. https://doi.org/10.25249/0375-7536.19956978

Singh, B., Sherman, D.M., Mosselmans, J.F.W., Gilkes, R.J., Wells, M.A., 2002. Incorporation of Cr, Mn and Ni into goethite (α-FeOOH): mechanism from extended X-ray absorption fine structure spectroscopy. Clay Miner. 37, 639–649. https://doi.org/10.1180/000985502374066

Sorensen, J. V., Gueguen, B., Stewart, B.D., Peña, J., Rouxel, O., Toner, B.M., 2020. Large nickel isotope fractionation caused by surface complexation reactions with hexagonal birnessite. Chem. Geol. 537. https://doi.org/10.1016/j.chemgeo.2020.119481

Spivak-Birndorf, L.J., Wang, S.J., Bish, D.L., Wasylenki, L.E., 2018. Nickel isotope fractionation during continental weathering. Chem. Geol. 476, 316–326. https://doi.org/10.1016/j.chemgeo.2017.11.028

Sun, J., Qin, H., Yang, S., Sanematsu, K., Takahashi, Y., 2022. New insights into the distribution and speciation of nickel in a Myanmar laterite. Chem. Geol. 604. https://doi.org/10.1016/j.chemgeo.2022.120943

Tassinari, C.C.G., Macambira, M.J.B., 1999. Geochronological provinces of the Amazonian Craton. Episodes 22, 174–182. https://doi.org/10.18814/epiiugs/1999/v22i3/004

Journal Pre-proof

Teixeira, A.S., Ferreira Filho, C.F., Giustina, M.E.S. Della, Araújo, S.M., da Silva, H.H.A.B., 2015. Geology, petrology and geochronology of the Lago Grande layered complex: Evidence for a PGE-mineralized magmatic suite in the Carajás Mineral Province, Brazil. J. South Am. Earth Sci. https://doi.org/10.1016/j.jsames.2015.09.006

Tupaz, C.A.J., Watanabe, Y., Sanematsu, K., Echigo, T., 2020. Mineralogy and geochemistry of the Berong Ni-Co laterite deposit, Palawan, Philippines. Ore Geol. Rev. 125, 103686. https://doi.org/10.1016/j.oregeorev.2020.103686

Ugwu, I.M., Sherman, D.M., Bacon, C.G.D., 2019. Sorption of nickel ontogoethite (α-FeOOH) and desorption kinetics of aged synthetic Ni-goethite: Implication for Ni laterite ore. Chem. Geol. 509, 223–233. https://doi.org/10.1016/j.chemgeo.2019.01.013

Ulrich, M., Cathelineau, M., Muñoz, M., Boiron, M.C., Teitler, Y., Karpoff, A.M., 2019. The relative distribution of critical (Sc, REE) and transition metals (Ni, Co, Cr, Mn, V) in some Ni-laterite deposits of New Caledonia. J. Geochemical Explor. 197, 93–113. https://doi.org/10.1016/j.gexplo.2018.11.017

Vasquez, M.L., Rosa-Costa, L.T., Silva, C., Ricci, P., Barbosa, J., Klein, E., Lopes, E., Macambira, E.M.B., Chaves, C., Carvalho, J., Oliveira, J., Anjos, G., Silva, H., 2008. Geologia e Recursos Mineirais do Estado do Pará: Sistema de Informações Geográficas - SIG. CPRM, Belém.

Villanova-de-Benavent, C., Domènech, C., Tauler, E., Galí, S., Tassara, S., Proenza, J.A., 2017. Fe–Ni-bearing serpentines from the saprolite horizon of Caribbean Ni-laterite deposits: new insights from thermodynamic calculations. Miner Deposita 52, 979–992. https://doi.org/10.1007/s00126-016-0683-7

Wang, S.J., Wasylenki, L.E., 2017. Experimental constraints on reconstruction of Archean seawater Ni isotopic composition from banded iron formations. Geochim. Cosmochim. Acta 206, 137–150. https://doi.org/10.1016/j.gca.2017.02.023

Wang, S. J., Wang, W., Zhu, J. M., Wu, Z., Liu, J., Han, G.,Li, W. (2021). Nickel isotopic evidence for late-stage accretion of Mercury-like differentiated planetary embryos. *Nature communications*, *12*(1), 1-7.

Wasylenki, L.E., Howe, H.D., Spivak-Birndorf, L.J., Bish, D.L., 2015. Ni isotope fractionation during sorption to ferrihydrite: Implications for Ni in banded iron formations. Chem. Geol. 400, 56–64. https://doi.org/10.1016/j.chemgeo.2015.02.007

Wiederhold, J.G., 2015. Metal stable isotope signatures as tracers in environmental geochemistry. Environ. Sci. Technol. 49, 2606–2624. https://doi.org/10.1021/es504683e

Journal Pre-proof

Nickel mass balance and isotopic records in a Serpentinic weathering profile: implications on the continental Ni budget

Table content

Journal Pre-proof

Table 1: Geochemical concentrations (wt.%) for major and relevant minor elements (Zr in mg kg^{-1}), isotopic compositions (δ^{60}Ni) and mass flux quantifications (ΔM_{Ni}). Values given in the table are the averages of each horizon.

Unit	Depth (m)	e$_2$O$_3$*	gO	iO$_2$	l$_2$O$_3$	r$_2$O$_3$	nO	iO	r	^{60}Ni	S.D.	M$_{Ni}$
		wt.%							g kg^{-1}		‰	cm^{-2}
limonite	0 - 4.2	2.89	45	3.14	.78	.58	.98	.06	4.31	0.46	.07	0.53
upper sap (top)	4.2 - 9.4	5.20	7.16	4.76	.19	.78	.32	.69	2.58	0.50	.07	.75
upper sap (bottom)		0.19	4.20	1.42	.29	.83	.30	.91	2.915	0.16	.07	.34
lower sap	9.4 - 24.6	4.33	9.45	5.37	.68	.45	.24	.72	.82	.28	.07	.22
saprock	24.6 - 45	0.16	3.23	3.35	.47	.38	.27	.39	.75	.26	.07	.d.
serpentinite	191	2.86	9.83	3.49	.84	.62	.16	.32	1.21	.25	.07	.d.

*Fe$_2$O$_3$ as total iron.

Journal Pre-proof

Nickel mass balance and isotopic records in a Serpentinic weathering profile: implications on the continental Ni budget

Figure caption:

Figure 1: **A)** Geographic location of Carajás Mineral Province. AM – Amazonian Craton; B – Borborema Province; M – Mantiqueira Province; SF – São Francisco Craton; T – Tocantins Province. **B)** Simplified geological map of Serra do Puma Complex (partially modified from Rosa, 2014). **C)** Geomorphic expression of the Serra do Puma and Serra da Onça nickel laterites in relationship to the Catetê River. The image is part of Sentinel-2A composite (true color, 4-3-2 band combination) available at https://earthexplorer.usgs.gov/ and treated in ESRI ArcGIS® 10.8 software. **D)** Typical Ni laterite profile from the SPC with characteristic assay results. The Red line represents Mg-discontinuity.

Figure 2: **A)** X-Ray diffraction results for a selection of representative samples. Chl – chlorite; Srp – serpentine; Px – Pyroxene; Ol. – Olivine; Cc – Calcite; Tlc – talc; Gibb – gibbsite; Gth – goethite; Hem – hematite; Qtz – quartz. **B)** Association of Fe oxyhydroxides and its boundary filled by quartz (N//; ~ 3.0 m); **C)** Association of Fe oxyhydroxides forming botryoidal features (N//; ~16 m); **D)** Saprock sample showing veins filled with calcite (NX; ~ 45 m); **E)** Dense serpentine matrix cut by veins filled by calcite (NX; ~ 45 m); **F)** Fibrous serpentine occupying almost the entirety of serpentinite thin section (NX; ~ 191 m). **G)** Pseudomorph olivine and pyroxene basal sections are almost entirely serpentinized (NX; ~ 181 m).

Figure 3: Geochemical results for major and relevant minor elements, and Ce/Ce* in the SPC profile. L – limonite; US – upper saprolite; LS – lower saprolite; SR – saprock. Serp. – serpentine; Qtz – quartz; Chr – chromite; Hem – hematite; Gth – goethite; Gibb – gibbsite; Lth – lithiophorite; Pyr – pyrolusite; Tlc – talc; Chl – chlorite; Corr – corrensite. Fe_2O_3 as total iron.

Figure 4: **A)** Computed gain and losses of Ni ($\tau_{Ni,w}$) calculated along the SPC weathering profile. **B)** Mass flux ΔM_{Ni} quantification in g cm^{-2} in relation to unaltered material. The green dashed line denotes the unweathered sample.

Figure 5: Fe, Mn, and Ni total and DCB extraction in g kg^{-1}. L – limonite; S – saprolite; SR – saprock. The Ni and Mn concentrations in LS and SR were below the detection limit.

Figure 6: Ni isotope values (δ^{60}Ni) in SPC weathering profile. The δ^{60}Ni value of the Bulk Silicate Earth at 0.23 ± 0.08 ‰ from Gall et al. (2017) is represented by a blue line with 2SD in lighter color.

Figure 7: Correlation between δ^{60}Ni and computed gain and losses ΔM_{Ni} showing that different processes may occur during weathering of ultramafic rocks of the SPC. The blue and green lines denote the Bulk Silicate Earth Ni isotopic composition (0.23 ± 0.08 ‰) from Gall et al. (2017) and the unaltered rock ($\Delta M = 0$). The grey circle highlights Ni-gain and heavy isotopic signature pool in the lower saprolite unit.

Journal Pre-proof

Figure 1

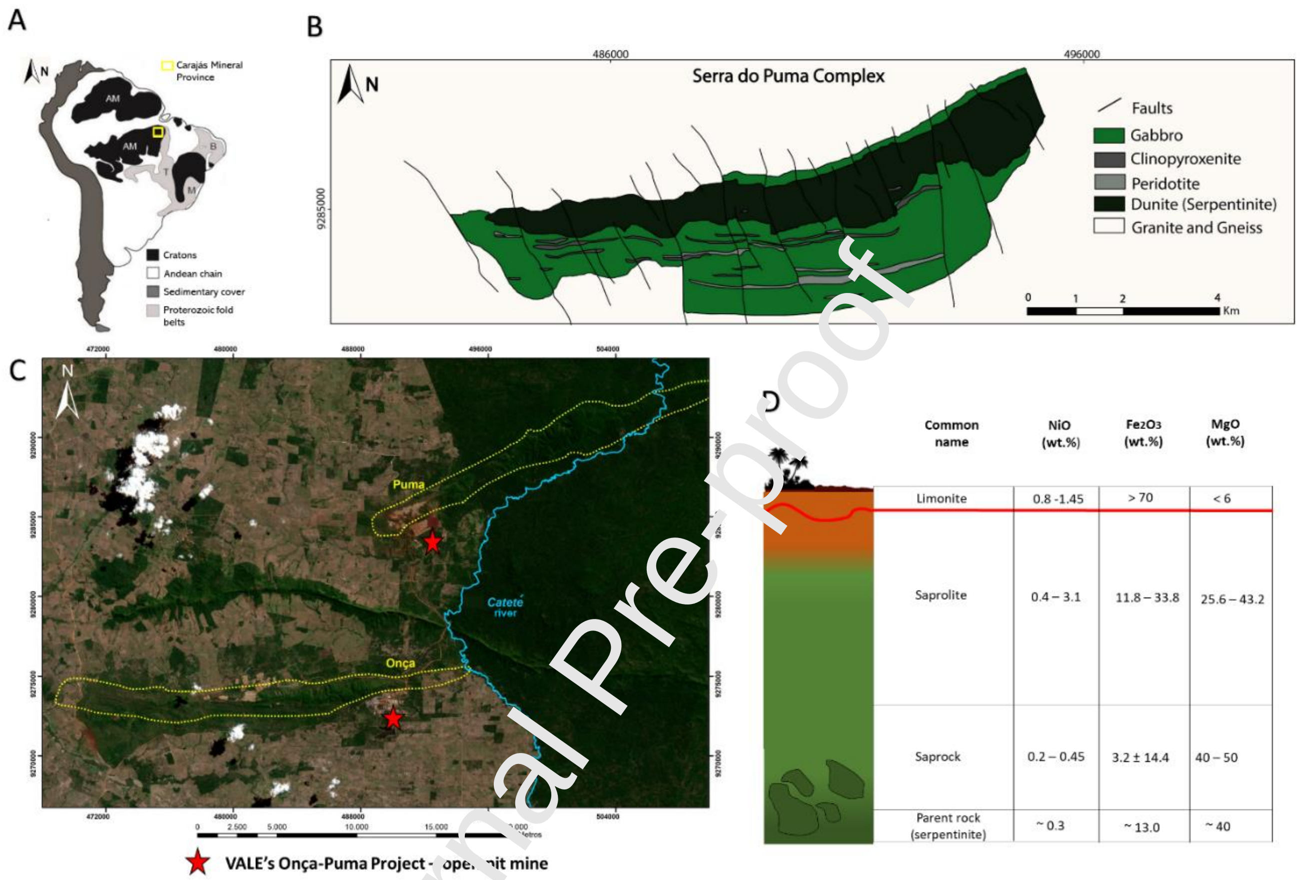

Common name	NiO (wt.%)	Fe_2O_3 (wt.%)	MgO (wt.%)
Limonite	0.8 -1.45	> 70	< 6
Saprolite	0.4 – 3.1	11.8 – 33.8	25.6 – 43.2
Saprock	0.2 – 0.45	3.2 ± 14.4	40 – 50
Parent rock (serpentinite)	~ 0.3	~ 13.0	~ 40

Journal Pre-proof

Figure 2

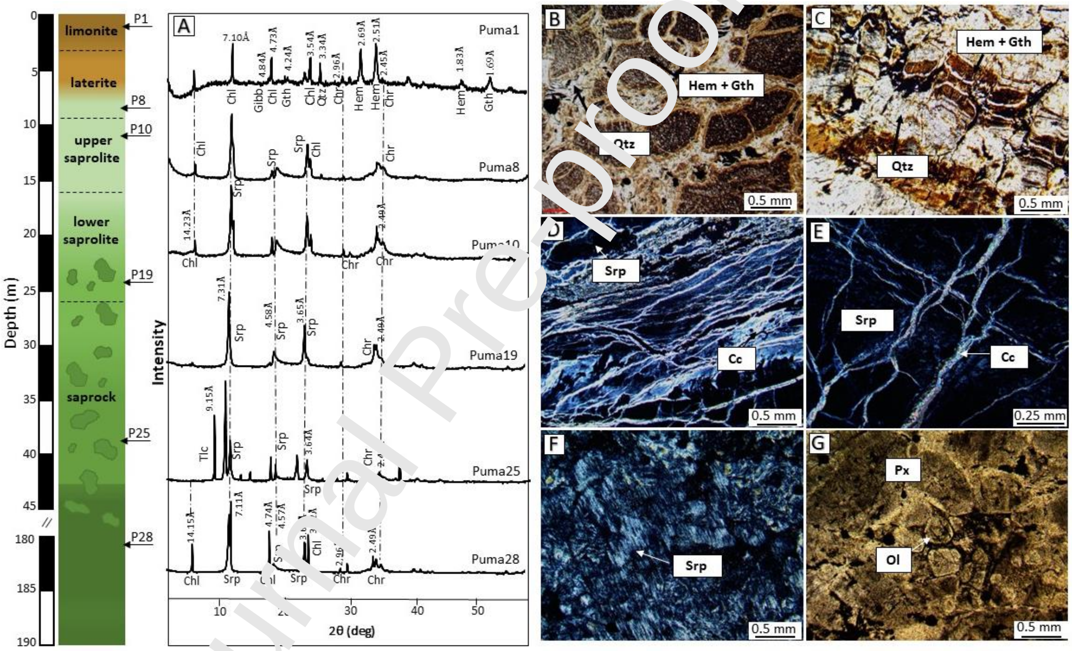

Journal Pre-proof

Figure 3

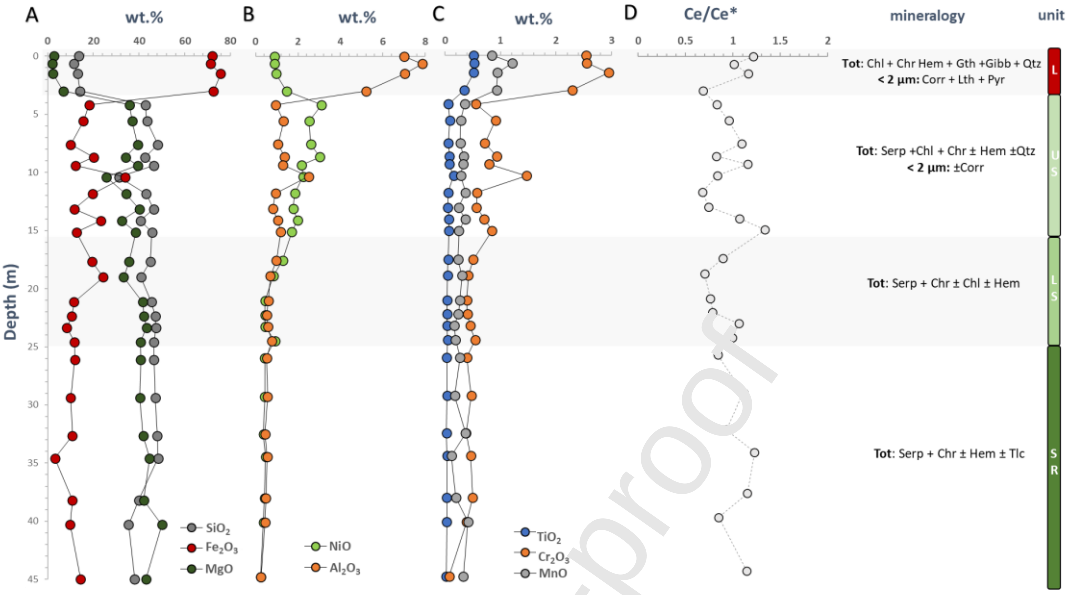

Journal Pre-proof

Journal Pre-proof

Figure 4

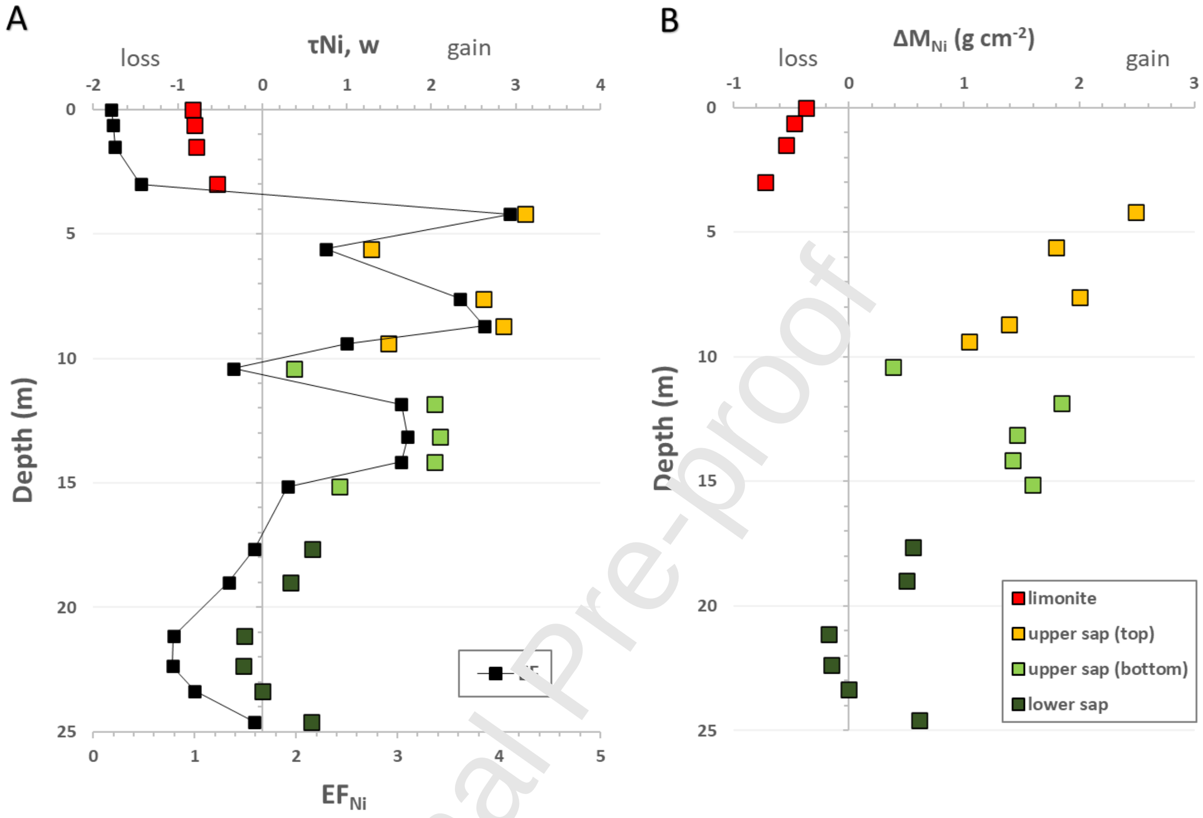

Journal Pre-proof

Figure 5

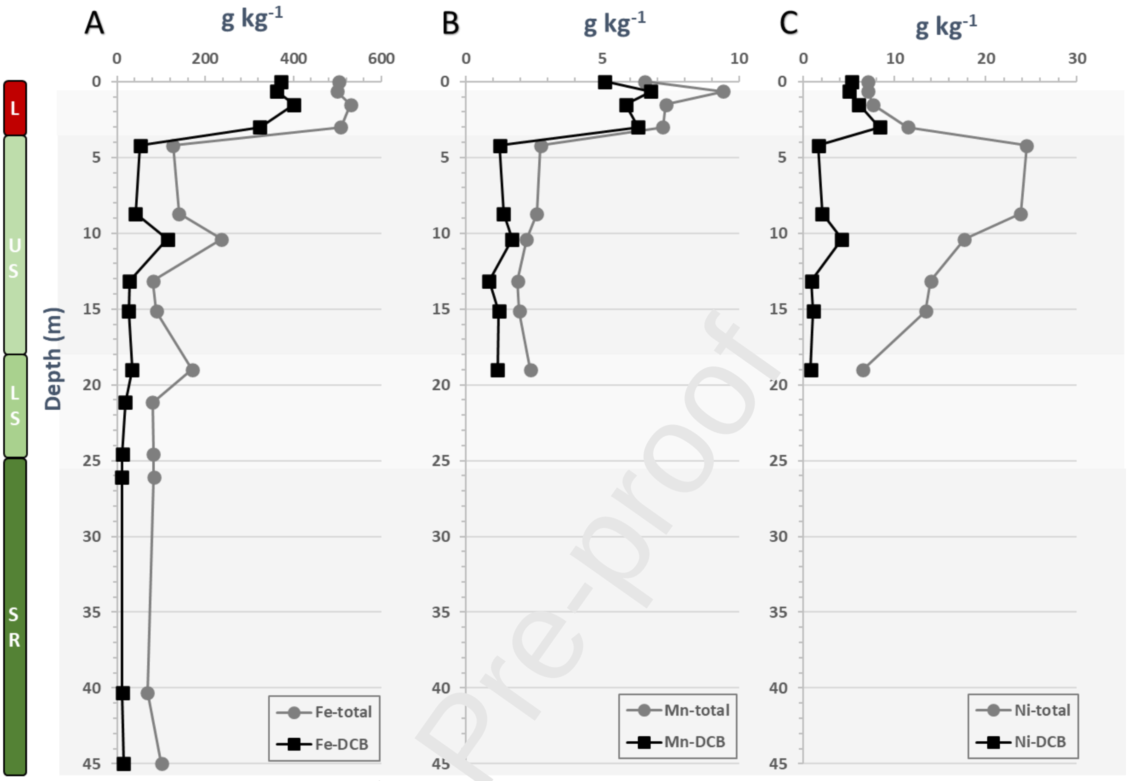

Journal Pre-proof

Figure 6

Journal Pre-proof

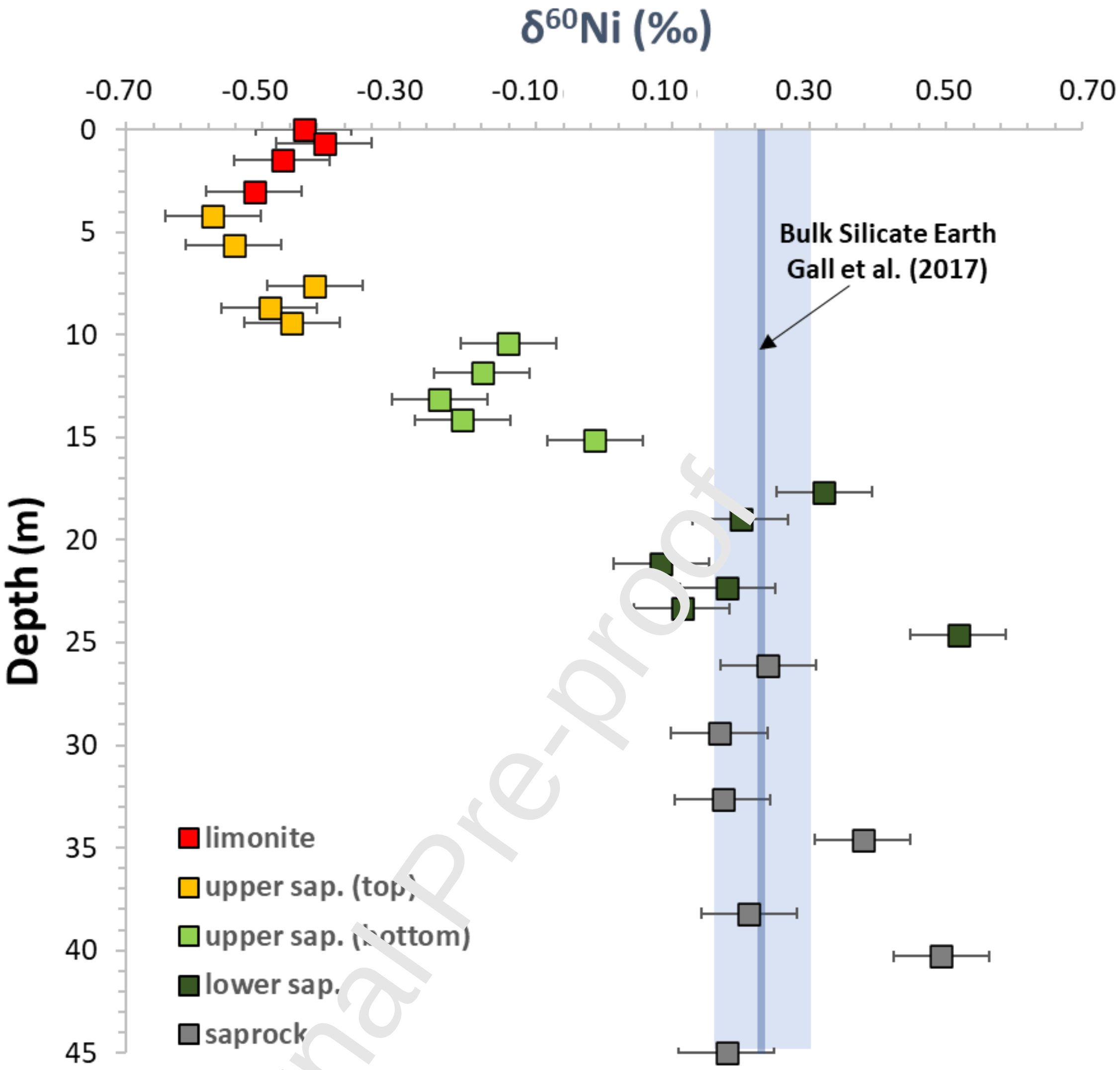

Journal Pre-proof

Figure 7

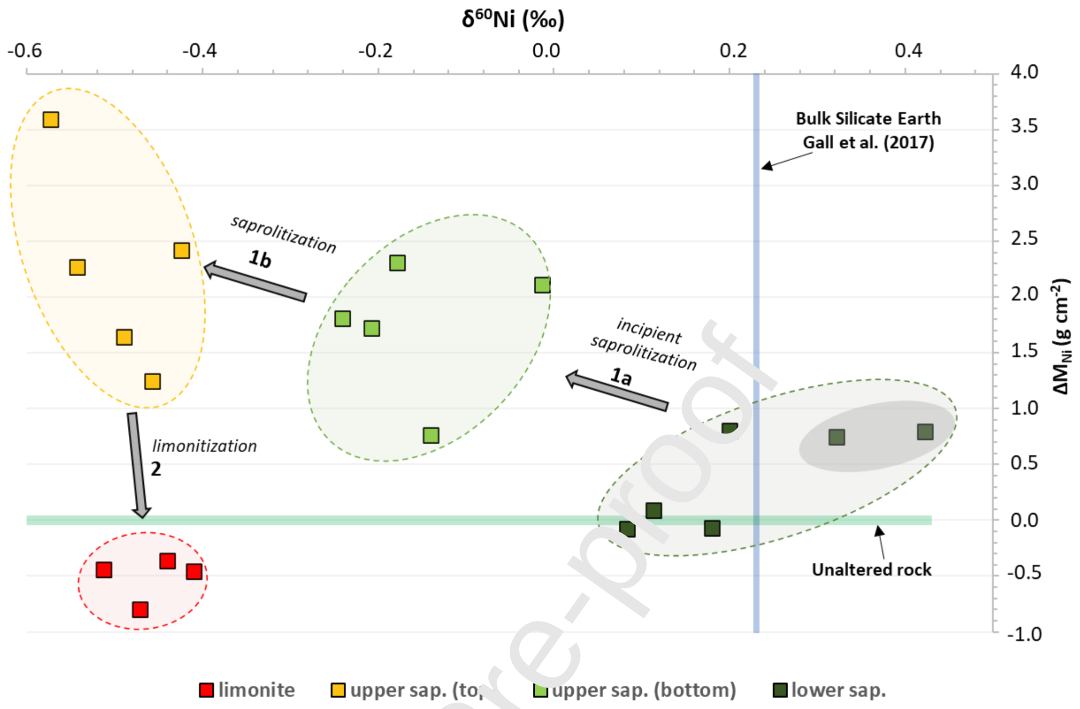

Journal Pre-proof

Declaration of interests

☒ The authors declare that they have no known competing financial interests or personal relationships that could have appeared to influence the work reported in this paper.

☐The authors declare the following financial interests/personal relationships which may be considered as potential competing interests:

Journal Pre-proof

Nickel mass balance and isotopic records in a Serpentinic weathering profile: implications on the continental Ni budget

Graphical abstract

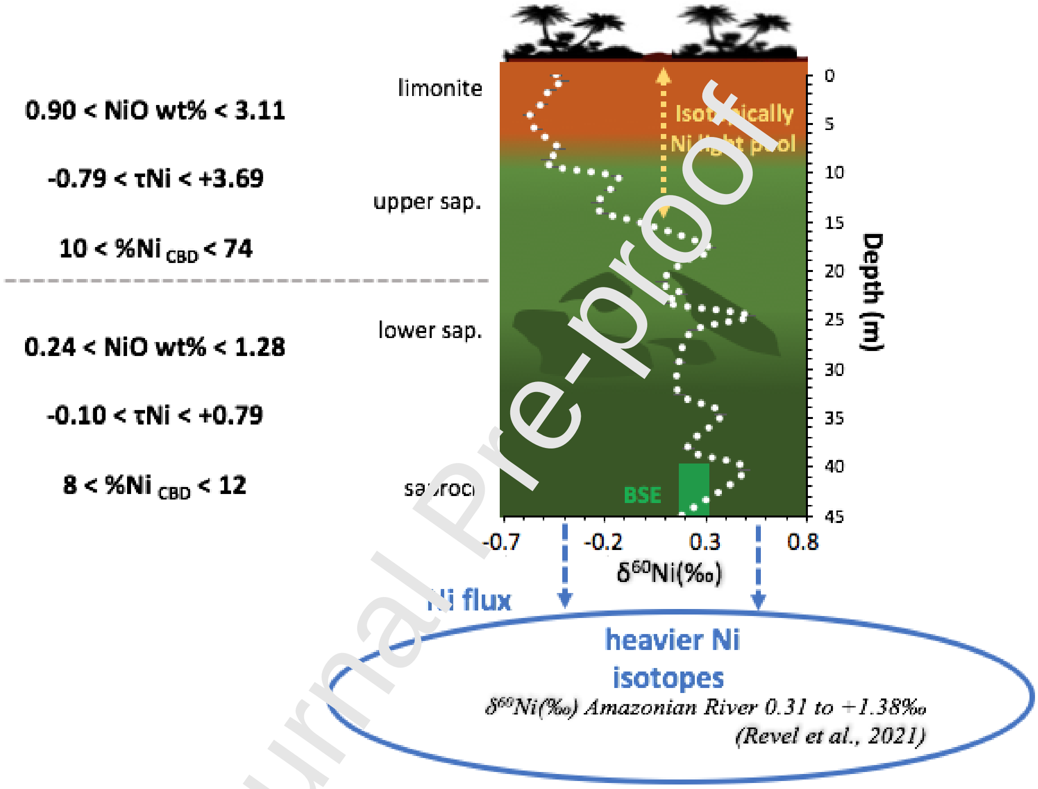

Journal Pre-proof

Nickel mass balance and isotopic records in a Serpentinic weathering profile: implications on the continental Ni budget

Highlights

- Serra do Puma Complex is structured in saprock, lower and upper saprolite, and limonite
- The upper saprolite represents the largest Ni residual enrichment zone
- Nickel isotopes in weathered serpentinite profiles record Ni fluxes and redistribution
- The weathering processes created an isotopically light Ni pool in the upper saprolite
- A large amount of heavy Ni isotope has been lost during weathering
- Evidence of a significant light Ni isotopes pool on the continent

Journal Pre-proof